Short-range correlations and meson exchange currents in photonucleon emission

M. Anguiano [1,2], G. Co' [1,2], A.M. Lallena [3] and S.R. Mokhtar [1,4]

[1)] Dipartimento di Fisica, Università di Lecce,
I-73100 Lecce, Italy

[2)] Istituto Nazionale di Fisica Nucleare sez. di Lecce,
I-73100 Lecce, Italy

[3)] Departamento de Física Moderna, Universidad de Granada,
E-18071 Granada, Spain

[4)] Department of Physics, University of Assiut,
Assiut, Egypt

Abstract

One-nucleon emission processes induced by photon absorption are studied by considering short-range correlations effects. At energies above the giant resonance region the validity of the direct knock-out model has been tested by comparison with continuum Random Phase Approximation results. Nucleon re-scattering effects have been considered by using an optical potential. The role of the electromagnetic convection, magnetization and meson exchange currents has been investigated as a function of both excitation energy and momentum transfer. The short-range correlation effects have been studied by using various correlation functions. We found that the nucleon photo-emission cross section is rather sensitive to the presence of short-range correlations at large values of nucleon emission angle. In this region, however, the effects of meson exchange currents are even larger than those produced by short-range correlations.

PACS number(s): 21.10.Ft, 21.60.-n

1 INTRODUCTION

The search for signatures of Short-Range Correlations (SRC) is one of the nuclear structure hot topics of these recent years. SRC are produced by the strong repulsive core of the bare nucleon-nucleon interaction. Medium-heavy nuclei are usually described with effective theories and interactions where the effects of the repulsive core, and therefore of the SRC, have been already tamed. The observation of effects clearly produced by SRC would set limits to the validity of the effective theories.

Perhaps the best known and most spectacular effect produced by the SRC is the increase of the nucleon momentum distribution at high momentum values with respect to the Independent Particle Model (IPM) predictions [1]-[4]. Unfortunately, the nucleon momentum distribution is not directly observable, therefore one has to search for phenomena sensitive to this quantity.

The first place to look for these phenomena is the nuclear ground state, the most investigated state from both experimental and theoretical point of view. Recently ground state calculations based on microscopic interactions, therefore considering SRC, have been provided also for medium-heavy nuclei [5]-[9]. It has been found that the SRC slightly modifies the charge distribution in the nuclear center, confirming the results of early calculations [10, 11]. However, the size of this effect is comparable to that produced by the coupling of low-lying collective phonons to the single particle wave functions [12] and therefore it is difficult to disentangle. No other ground state observables showing relevant sensitivity to the SRC have been found, therefore one has to search for processes involving the excitation of the nuclear system.

The status of the theory in the description of nuclear excited states is not so well advanced as in the case of the ground state. In these last years we have developed a model which considers SRC in the description of nuclear excited states [13]-[17]. Our work is based on the nuclear matter model of Ref. [18] used to study inclusive responses [19] and spectral functions [20]. With respect to this model we made an additional approximation consisting in cutting the cluster expansion at the first order in the correlation line. A detailed presentation of our approach is given in Ref. [16] where it has been applied to the description of the quasi-elastic inclusive responses. Recently, we extended the model to investigate (e,e'p) reactions [17], and in the present paper we use it to study one-nucleon emission processes induced by photon absorption.

The two main approximations of our model are the exclusion of the diagrams containing more than one correlation line, and the neglect of collective excitations of the nucleus, such as the surface vibrations. The first approximation has been tested in Ref. [14] by comparing our nuclear matter quasi-elastic charge responses with those obtained with a complete Correlated Basis Function calculation [18, 19]. The agreement between the two calculations is excellent.

The second approximation has limited the application of our model to situations where collective excitations can be neglected. In Ref. [15] we calculated discrete excitations which can be rather well described in terms of single particle excitations. In [13, 16] and [17] we applied our model in the quasi-elastic kinematic regime, dominated by one-particle

one-hole (1p-1h) excitations [21].

The characteristic kinematic conditions which in electron scattering ensured that collective effects were negligible (high values of the momentum transfer for a fixed excitation energy), cannot be achieved with real photons. For this reason we felt necessary to study the importance of collective excitation modes in photo-reactions. We have done this investigation by using the continuum Random Phase Approximation (RPA) theory, and we found that collective excitations can be neglected, above the giant resonance region. As in the electron scattering case, the largest correction to the naive mean field model arises from the rescattering of the emitted nucleon with the rest nucleus. This final state interaction can be described rather well within an optical model framework.

After establishing validity and limitations of the direct knock-out model, we have investigated the role of electromagnetic currents operators used in the calculations. In the energy region of interest we found that it is safer to use the explicit form of the convection current rather than employing the long wave approximation. Furthermore it is necessary to include the magnetization current. The contribution of Meson Exchange Currents (MEC) generated by the exchange of pions has been investigated with the method used in Refs. [22, 23] to study the quasi-elastic (e,e') responses. We have obtained MEC effects smaller than those presented in the literature. However they are relevant and cannot be neglected.

After testing the validity of the model and the role of the electromagnetic operators, we started our investigation of the SRC. In our calculations the SRC act only on the one-body (OB) operators, therefore MEC and correlations interact only through the interference between the transition amplitudes. We used purely scalar (Jastrow) correlation functions fixed in Fermi Hypernetted Chain (FHNC) calculations done with semi-realistic [8] and realistic [9] nucleon-nucleon interactions. The consistency between the hole single particle wave functions and the correlation functions, is provided by the the minimization procedure used in the FHNC calculations.

All our calculations have been done for the ^{16}O nucleus. This is a light doubly closed shell nucleus and it has been widely investigated from the theoretical point of view. At the same time a large set of experimental data is available in the literature. These facts allow us to compare our results for various kinematic conditions with those of other theories and with experimental data. Furthermore there are also (e,e'p) data we can use to test our model.

The paper is mainly focused on the numerical results. Details of the correlated model and of the MEC treatment are given in Refs. [16] and [22, 23] respectively. Here we discuss briefly the extension of the model to the case of the photonuclear reactions in Sects. 2 and 3. The applications of our model are presented in Sect. 4 which has been divided in various parts following the logical path above described: first we present the investigation about collective modes (Sect. 4.1), then about the currents (Sect. 4.2) followed by the study of the SRC effects (Sect. 4.3) and finally by the comparison with the data (Sect. 4.4). In the last section we summarize the results and draw our conclusions.

2 THE CROSS SECTIONS

In this section we briefly recall the expressions used to evaluate the cross section for the nucleon emission induced by the absorption of a photon. Detailed derivations of these expressions can be found in review articles [24] and books [25, 26]. We work in natural units ($\hbar = c = 1, e^2 = 1/137.04$) and employ the conventions of Bjorken and Drell [27].

The basic quantity to calculate is the transition amplitude

$$R_T(q,\omega) \;=\; \sum_{\eta=\pm 1} \left|\langle \Psi_f|\, J_\eta(q)\, |\Psi_i\rangle\right|^2 \,\delta(E_f - E_i - \omega)\,, \tag{1}$$

where we have indicated with $|\Psi_i\rangle$ and $|\Psi_f\rangle$ the initial and final nuclear states and with E_i and E_f their energies. In the above expression we show the dependence of transition amplitude on q and ω, the modulus of the momentum and the energy transferred to the nucleus. In electron scattering processes, by neglecting the electron rest mass, one has $\epsilon_i - \epsilon_f \leq q \leq \epsilon_i + \epsilon_f$ where ϵ_i and ϵ_f are the initial and final energies of the electron. In processes involving real photons one has $\omega = q = \epsilon_i - \epsilon_f = E_f - E_i$. Another difference between processes involving electrons and real photons is that in the last case the longitudinal term of the electromagnetic current, related to the nuclear charge distribution, does not contribute. For this reason in Eq. (1) only the transverse components of the current appear

$$J_\pm = \mp \frac{1}{\sqrt{2}} \left(J_x \pm i J_y\right)\,. \tag{2}$$

The nuclear initial state is characterized by the total angular momentum and parity of the system. Since we restrict our calculations to doubly closed shell nuclei we immediately consider that the nuclear ground state has zero angular momentum and positive parity $|\Psi_i\rangle \equiv |\Psi; J_i M_i; \Pi_i\rangle = |\Psi; 00; +1\rangle$. In processes where the emitted nucleon is detected, the nuclear final state can be described as [17, 28, 29]

$$\begin{aligned} |\Psi_f\rangle \;\;=\;\; & \frac{4\pi}{|\mathbf{p}|} \sum_{l_p\mu_p} \sum_{j_p m_p} \sum_{JM,\Pi} i^{l_p} Y^*_{l_p\mu_p}(\widehat{\mathbf{p}}) \langle l_p \mu_p \frac{1}{2} \sigma | j_p m_p\rangle \\ & \langle j_p m_p j_h m_h | JM\rangle \, |\Psi; JM; \Pi; (l_p j_p m_p \epsilon_p, l_h j_h m_h \epsilon_h)\rangle\,. \end{aligned} \tag{3}$$

In the above equation $|\Psi; JM; \Pi; (l_p j_p m_p \epsilon_p, l_h j_h m_h \epsilon_h)\rangle$ describes the excited state of the A nucleons system with total angular momentum J, $z-$axis projection M and parity Π. This state is composed by a particle in the continuum wave characterized by orbital and total angular momenta l_p and j_p, respectively, with projection m_p, energy ϵ_p and momentum $\mathbf{p}$, and a residual nucleus with hole quantum numbers l_h j_h, m_h and ϵ_h. With the symbol $Y_{l\mu}$ we indicated the spherical harmonics and with $\langle l_a m_a l_b m_b | JM\rangle$ the Clebsch-Gordan coefficients [30]. Using the above definitions we express the transition amplitude as [17, 28, 29]

$$R_T(q,\omega) \;= \frac{32\pi^3}{|\mathbf{p}|^2} \sum_{\sigma m_h} \sum_{J\Pi l_p j_p} \sum_{J'\Pi' l'_p j'_p} \sum_{\eta \pm 1} (-i)^{l_p - l'_p - J + J'} \frac{1}{\sqrt{2J+1}} \frac{1}{\sqrt{2J'+1}}$$

$$\langle l_p \mu_p \frac{1}{2} \sigma | j_p m_p \rangle \langle j_p m_p j_h m_h | J - \eta \rangle \langle l'_p \mu_p \frac{1}{2} \sigma | j'_p m'_p \rangle \langle j'_p m_p j_h m_h | J' - \eta \rangle$$
$$\left[\frac{(l_p + m_h + \eta + \sigma)!}{(l_p - m_h - \eta - \sigma)!} \frac{(l'_p + m_h + \eta + \sigma)!}{(l'_p - m_h - \eta - \sigma)!} \right]^{\frac{1}{2}} \left[\frac{2l_p + 1}{4\pi} \right]^{\frac{1}{2}} \left[\frac{2l'_p + 1}{4\pi} \right]^{\frac{1}{2}}$$
$$P_{l_p}^{\mu_p}(\cos\Theta)\ P_{l'_p}^{\mu_p}(\cos\Theta)\ \xi_{J,M,\eta,\Pi}(q;p,h)\ \xi^{\dagger}_{J',M',\eta,\Pi'}(q;p',h)\,\delta(\epsilon_p - \epsilon_h - \omega)\,. \qquad (4)$$

In the above expression we have defined

$$\xi_{J,M,\eta,\Pi}(q,\omega;p,h) = \langle \Psi; JM; \Pi(l_p j_p m_p \epsilon_p, l_h j_h m_h \epsilon_h) |\, J_{\eta,JM}(q,\omega)\, |\Psi; 00; +1\rangle \qquad (5)$$

and we made explicit the dependence on the associate Legendre polynomials P_l^{μ}.

With the above definitions the cross section describing the nucleon emission induced by the absorption of a photon can be written as [24]

$$\frac{\mathrm{d}\sigma(\omega)}{\mathrm{d}\Omega} = \frac{2\pi^2 e^2}{\omega}\ \frac{|\mathbf{p}| M}{(2\pi)^3}\ R_T(q=\omega,\omega)\,, \qquad (6)$$

where M is the emitted nucleon rest mass.

In the inclusive total photoabsorption cross section the emitted nucleon is not detected. The cross section for this process is obtained from the expression (6) by summing all the emission channels and integrating on all the possible directions of the emitted nucleon [31]

$$\begin{aligned} \sigma(\omega) &= \sum_{l_p j_p m_p} \sum_{l_h j_h m_h} \int \mathrm{d}\Omega \frac{\mathrm{d}\sigma(\omega)}{\mathrm{d}\Omega} \\ &= \frac{8\pi^3 e^2}{\omega} \sum_{\eta,J,M,\Pi} \sum_{p,h} |\xi_{J,M,\eta,\Pi}(q=\omega,\omega;p,h)|^2\, \delta(\epsilon_p - \epsilon_h - \omega)\,. \end{aligned} \qquad (7)$$

The last equation shows that, in the total photoabsorption cross section, the nucleus is considered to make a transition from its ground state to an excited state with good angular momentum and parity. The interference between the excitation multipoles in Eq. (4) vanishes because of the integration on θ_p and the orthogonality of the Legendre polynomials.

In Eq. (5) we have introduced the multipole operator $J_{\eta,JM}$, which comes from the corresponding current expansion and which is conveniently described as sum of the electromagnetic operators $T^{\mathrm{E}}_{JM}(q)$ and $T^{\mathrm{M}}_{JM}(q)$ which generate, respectively, electric and magnetic excitations [22, 23]. These operators are defined as

$$T^{\mathrm{E}}_{JM}(q) = \frac{1}{\omega} \int \mathrm{d}^3 r \left\{ \nabla \times \left[j_J(qr)\, \mathbf{Y}^M_{JJ}(\hat{\mathbf{r}}) \right] \right\} \cdot \mathbf{J}(\mathbf{r}) \qquad (8)$$

and

$$T^{\mathrm{M}}_{JM}(q) = \int \mathrm{d}^3 r\, j_J(qr)\, \mathbf{Y}^M_{JJ}(\hat{\mathbf{r}}) \cdot \mathbf{J}(\mathbf{r})\,, \qquad (9)$$

where we have indicated with $j_J(qr)$ the spherical Bessel function, with $\mathbf{Y}^M_{JJ}$ the vector spherical harmonics [30], and with $\mathbf{J}(\mathbf{r})$ the electromagnetic current operator. We suppose

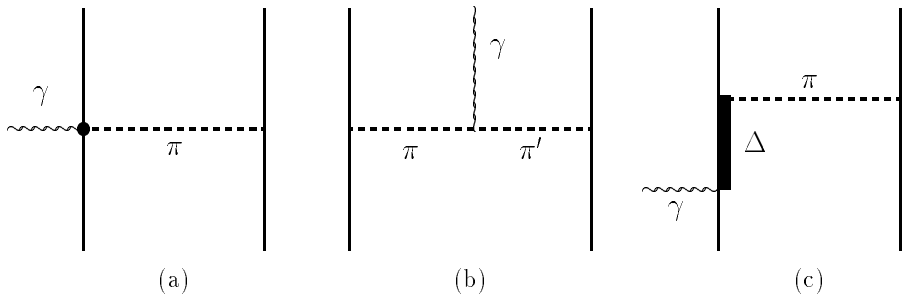

Figure 1: Feynman diagrams of the three MEC operators we consider: (a) seagull, (b) pionic and (c) Δ isobar.

that this operator is composed by the sum of one- and two-body operators, these last ones produced by the exchange of mesons.

The OB current is the sum of the convection

$$\mathbf{j}^c(\mathbf{r}) \,=\, \sum_{k=1}^{A} \frac{1}{i2M_k} \frac{1+\tau_3(k)}{2} \left[\delta(\mathbf{r}-\mathbf{r}_k)\,\nabla_k \,+\, \nabla_k\,\delta(\mathbf{r}-\mathbf{r}_k)\right] \tag{10}$$

and magnetization

$$\mathbf{j}^m(\mathbf{r}) \,=\, \sum_{k=1}^{A} \frac{1}{M_k} \left(\mu_P \frac{1+\tau_3(k)}{2} + \mu_N \frac{1-\tau_3(k)}{2}\right) \nabla_k \times \delta(\mathbf{r}-\mathbf{r}_k)\,\boldsymbol{\sigma}(k) \tag{11}$$

currents. In the above equations M_k indicates the mass of the k-th nucleon, μ_P and μ_N the anomalous magnetic moments of the proton and neutron respectively, $\boldsymbol{\sigma}(k)$ the Pauli matrices and $\tau_3(k) = 1$ if the k-th nucleon is a proton and $\tau_3(k) = -1$ in case it is a neutron.

The above expressions refer to point-like nucleons. In actual calculations we folded them with the electric and magnetic nucleon form factors, $G^{\mathrm{P,N}}_{\mathrm{E,M}}(q,\omega)$. We used the parameterization of Ref. [32].

To give the expressions of the MEC it is convenient to define the function $h(\mathbf{r})$ as the Fourier transform of the dynamical pion propagator [23]

$$h(\mathbf{r}-\mathbf{r}_l) = \int \frac{\mathrm{d}^3k}{(2\pi)^3} \frac{F_{\pi\mathrm{N}}(k,\varepsilon)\,\mathrm{e}^{i\mathbf{k}\cdot(\mathbf{r}-\mathbf{r}_l)}}{k^2+m_\pi^2-\varepsilon^2}\,, \tag{12}$$

where we have indicated with $F_{\pi\mathrm{N}}$ the pion–nucleon form factor and with $\varepsilon = (\Delta E)_l$ the energy of the exchanged pion, of mass m_π, obtained as the difference between the energies of the final and initial single particle states of the l-th nucleon.

In our work we consider the three types of MEC represented by the Feynman diagrams of Fig. 1. They are the seagull (a), the pionic (b) and the virtual Δ excitation (c) terms. The expressions of the seagull and pionic currents are, respectively,

$$\mathbf{j}^{\mathrm{S}}(\mathbf{q},\omega) = 4\pi \frac{f_\pi^2}{m_\pi^2}\, F_{\mathrm{S}}(q,\omega) \sum_{\substack{k,l=1\\k\neq l}}^{A} \left[\boldsymbol{\tau}(k)\times\boldsymbol{\tau}(l)\right]_3 \mathrm{e}^{i\mathbf{q}\cdot\mathbf{r}_k} \boldsymbol{\sigma}(k)\,\boldsymbol{\sigma}(l)\cdot\nabla_k h(\mathbf{r}_k-\mathbf{r}_l)\,, \tag{13}$$

and

$$\mathbf{j}^{\pi}(\mathbf{q},\omega) \;=\; -4\pi\frac{f_\pi^2}{m_\pi^2}\,F_\pi(q,\omega)\sum_{\substack{k,l=1\\k\neq l}}^{A}[\boldsymbol{\tau}(k)\times\boldsymbol{\tau}(l)]_3\int \mathrm{d}^3r\,\mathrm{e}^{i\mathbf{q}\cdot\mathbf{r}}$$
$$\boldsymbol{\sigma}(k)\cdot\nabla h(\mathbf{r}-\mathbf{r}_k)\,\nabla\,[\boldsymbol{\sigma}(l)\cdot\nabla h(\mathbf{r}-\mathbf{r}_l)]\;. \tag{14}$$

The situation for the Δ–isobar current is not so well defined because formulations based upon static quark models [33, 34] or chiral lagrangian [35, 36] give different expressions. We have adopted the point of view of the first group of authors and use the expression

$$\mathbf{j}^{\Delta}(\mathbf{q},\omega) \;=\; -iC_\Delta F_\Delta(q,\omega)\sum_{\substack{k,l=1\\k\neq l}}^{A}\mathrm{e}^{i\mathbf{q}\cdot\mathbf{r}_k}\mathbf{q}$$
$$\Big\{[\boldsymbol{\tau}(k)\times\boldsymbol{\tau}(l)]_3\,\boldsymbol{\sigma}(k)\times\nabla_k\,\boldsymbol{\sigma}(l)\cdot\nabla_k\,h(\mathbf{r}_k-\mathbf{r}_l)\;-\;4\tau^3(l)\,\nabla_k\,\boldsymbol{\sigma}(l)\cdot\nabla_k\,h(\mathbf{r}_k-\mathbf{r}_l)\Big\}\;.$$

In the above equations $f_\pi = 0.079$ is the effective pion-nucleon coupling constant and

$$C_\Delta = 4\pi\frac{f_\pi^2}{m_\pi^2}\,\frac{4}{25M(M_\Delta - M)}\,, \tag{15}$$

with M_Δ the Δ mass. We have indicated with the symbols F_π, F_Δ the electromagnetic form factors of the pion and of the Δ and with F_S the electric isovector nucleon form factor. To be consistent with the one-body currents we used the following expressions for F_S and F_π

$$F_{\mathrm{S}}(q,\omega) \;=\; G_{\mathrm{E}}^{\mathrm{P}}(q,\omega) - G_{\mathrm{E}}^{\mathrm{N}}(q,\omega), \tag{16}$$
$$F_\pi(q,\omega) \;=\; F_{\pi\gamma}(q,\omega) = \frac{1}{1+(q^2-\omega^2)/m_\rho^2}\,, \tag{17}$$

where m_ρ is the mass of the ρ-meson.

The situation is more complicated for the Δ current since the electromagnetic form factor F_Δ, and the constant C_Δ are model dependent. The major uncertainty is related to C_Δ, but a discussion of this problem is beyond the aim of the present work. The expression (15) of C_Δ we have chosen is widely used in the literature [34, 37]. For the form factor F_Δ, following the static quark model, we have used

$$F_\Delta(q,\omega) \;=\; 2G_{\mathrm{M}}^{V}(q,\omega) \;=\; G_{\mathrm{M}}^{\mathrm{P}}(q,\omega) - G_{\mathrm{M}}^{\mathrm{N}}(q,\omega)\,. \tag{18}$$

Finally, we would like to comment on the pion-nucleon form factor

$$F_{\pi\mathrm{N}}(k,\varepsilon) = \frac{\Lambda^2 - m_\pi^2}{\Lambda^2 + k^2 - \varepsilon^2} \tag{19}$$

included in the expression (12) of the pion propagator. We have verified [22] that, in the quasi-elastic peak region, for the values of Λ commonly accepted (~ 1 GeV), the results are very close to those obtained considering simply $F_{\pi\mathrm{N}} = 1$, which is the value we have adopted.

3 THE NUCLEAR MODEL

In the previous section we have described the reaction mechanism but we did not specify the structure of the nuclear ground excited states. These are the two inputs required to calculate the ξ functions in Eq. (5).

Because of energy conservation, the knowledge of the energy, and of the momentum, of the emitted nucleon identifies the quantum numbers of the hole state of the residual nucleus. The state $|\Psi; JM; \Pi; (l_p j_p m_p \epsilon_p, l_h j_h m_h \epsilon_h)\rangle$ is asymptotically characterized by the quantum numbers of a 1p-1h excitation we label generically with p and h.

In our model the nuclear states are described as

$$|\Psi; 00; +1\rangle = \frac{F\ |\Phi; 00; +1\rangle}{\langle \Phi; 00; +1|\ F^\dagger F\ |\Phi; 00; +1\rangle^{\frac{1}{2}}}\ , \tag{20}$$

$$|\Psi; JM; \Pi; p, h\rangle = \frac{F\ |\Phi; JM; \Pi; p, h\rangle}{\langle \Phi; JM; \Pi; p, h|\ F^\dagger F\ |\Phi; JM; \Pi; p, h\rangle^{\frac{1}{2}}}\ . \tag{21}$$

We have indicated with $|\Phi; 00; +1\rangle$ the Slater determinant describing the mean field wave function in a pure IPM. This means that, given a basis of single particle wave functions, all the states below the Fermi surface are fully occupied and those above are all completely empty. The state $|\Phi; JM; \Pi; ph\rangle$ indicates a Slater determinant where the hole function h has been substituted with the continuum particle function p. With respect to the IPM, the novelty of our ansatz is the presence of the correlation function F. This function has, in principle, a very complicated operatorial dependence, analogous to that of the hamiltonian [9, 38]. In this work we restrict our calculations to the case of purely scalar (Jastrow) correlations, therefore we immediately simplify the expressions formulating them only in terms of this type of correlations. The adopted ansatz about the correlation is [39]

$$F(1, 2, ...A) = \prod_{i<j}^{A} f(r_{ij})\ , \tag{22}$$

where $r_{ij} = |\mathbf{r}_i - \mathbf{r}_j|$ is the distance between the the particles i and j.

In order to make use of well-established cluster expansion techniques [18] we rewrite the transition matrix $\xi_{J,M,\eta,\Pi}(q, \omega = \epsilon_p - \epsilon_h; p, h)$ in Eq. (5) as

$$\xi_{J,M,\eta,\Pi}(q, \epsilon_p - \epsilon_h; p, h) = \frac{\langle \Psi; JM; \Pi; p, h|J_{\eta,JM}(q)|\Psi; 00; +1\rangle}{\langle \Psi; 00; +1|\Psi; 00; +1\rangle} \left[\frac{\langle \Psi; 00; +1|\Psi; 00; +1\rangle}{\langle \Psi; JM; \Pi; p, h|\Psi; JM; \Pi; p, h\rangle}\right]^{\frac{1}{2}}\ . \tag{23}$$

The two factors in Eq. (23) are separately evaluated by expanding both numerator and denominator in powers of the short-range correlation function. The presence of the denominators is used to eliminate the unlinked diagrams [18].

The matrix element to be calculated in Eq. (23) is

$$\begin{aligned}
&\langle \Psi; JM; \Pi; p, h | J_{\eta,JM}(q) | \Psi; 00; +1 \rangle \\
&\qquad = \langle \Phi; JM; \Pi; p, h | F^\dagger J_{\eta,JM}(q) F | \Phi; 00; +1 \rangle_L \\
&\qquad = \langle \Phi; JM; \Pi; p, h | J_{\eta,JM}(q) \prod_{i<j}^{A} f^2(r_{ij}) | \Phi; 00; +1 \rangle_L \\
&\qquad = \langle \Phi; JM; \Pi; p, h | J_{\eta,JM}(q) \prod_{i<j}^{A} (1 + h_{ij}) | \Phi; 00; +1 \rangle_L \,, \qquad (24)
\end{aligned}$$

where we have used the function $h_{ij} = f^2(r_{ij}) - 1$ and the subindex L indicates that only the linked diagrams are considered.

Up to this moment the treatment of the transition matrix element is the same as that adopted in nuclear matter [18, 19]. We insert at this point a new approximation consisting in retaining only those terms where the h_{ij} function appears only once

$$\begin{aligned}
\xi_{J,M,\eta,\Pi}(q, \epsilon_p - \epsilon_h; p, h) \;&\longrightarrow\; \xi^1_{J,M,\eta,\Pi}(q, \epsilon_p - \epsilon_h; p, h) \\
&= \langle \Phi; JM; \Pi; p, h | \, J_{\eta,JM}(q) \sum_{i<j} (1 + h_{ij}) \, | \Phi; 00; +1 \rangle_L \,. \qquad (25)
\end{aligned}$$

This result has been obtained using a procedure analogous to that adopted in Ref. [11] to evaluate the density distribution, therefore the truncation of the expansion is done only after the elimination of the unlinked diagrams.

By identifying with 1 the coordinate of the nucleon struck by the photon, we can express the ξ^1 in Eq. (25) as

$$\begin{aligned}
\xi^1_{J,M,\eta,\Pi}(q, \epsilon_p - \epsilon_h; p, h) \;&=\; \langle \Phi; JM; \Pi; p, h | \, J_\eta(q) \, | \Phi; 00; +1 \rangle \\
&\quad + \langle \Phi; JM; \Pi; p, h | \, J_\eta(q) \sum_{j>1}^{A} h_{1j} \, | \Phi; 00; +1 \rangle_L \\
&\quad + \langle \Phi; JM; \Pi; p, h | \, J_\eta(q) \sum_{1<i<j}^{A} h_{ij} \, | \Phi; 00; +1 \rangle_L \,. \qquad (26)
\end{aligned}$$

The various terms generated by the above expression are shown as Mayer-like diagrams [40] in Fig. 2. The first term in Eq. (26) is the IPM contribution and it corresponds to the one-point diagram (1.1) of Fig. 2. The other two terms in Eq. (26) are represented by the two- and three-point diagrams. The presence of these last diagrams is necessary to have the correct normalization of the many-body wave function, as discussed in [16].

What should be specified now is the set of single particle wave functions and the correlation functions. We took them from the FHNC calculations of Refs. [8, 9] where these ingredients of the calculation have been fixed by minimizing the ground state expectation value of the hamiltonian. In Ref. [8] the set of single particle wave functions was taken from the literature [28, 29] and the minimization was done only by changing the correlation. This procedure was justified because the nucleon–nucleon interaction was

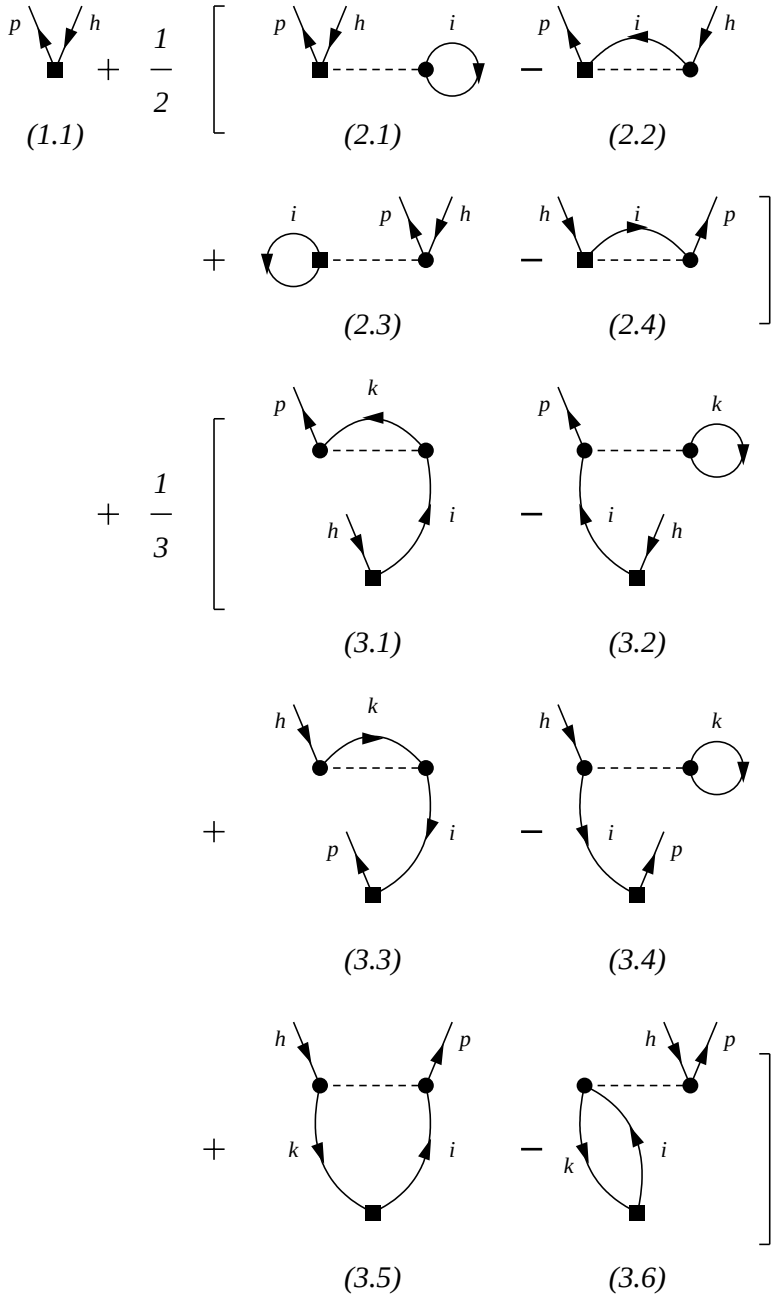

Figure 2: Mayer-like diagrams describing the SRC considered in our calculations.

semi-realistic. In the calculations of the present work we have used the correlations obtained with the S3 interaction of Afnan and Tang [41] by means of the Euler and gaussian procedures (see Ref. [8]). For sake of comparison in our calculations we have also used the scalar part of the state dependent correlation function fixed in Ref. [9].

The calculations of the transition matrix elements are carried out by performing a multipole expansion of the correlation function h_{ij} [11, 16, 17]. The single particle wave functions are described in a spherical basis, and we used the traditional angular momentum coupling techniques to evaluate the matrix elements. The explicit expressions of these matrix elements for the magnetization current are given in Ref. [16]. Those of the convection current are given in Ref. [42].

The MEC have have been calculated only in the IPM, i. e. neglecting the last two terms in Eq. (26). Their expressions are given in Refs. [22, 23, 43]. As already stated in the introduction, in our computational scheme SRC and MEC are related only by the interference terms of the transition matrix elements.

4 SPECIFIC APPLICATIONS

The nuclear model above presented has been applied to describe nucleon emission from the ^{16}O nucleus. The motivations of this choice have already been outlined in the introduction. It is a spherical doubly-closed shell nucleus and the implied symmetries simplify the treatment of shell and finite size effects. For these reasons the ground state of this nucleus has been the subject of investigation of microscopic theories [6]-[9]. Also our calculations relative to inclusive [16] and exclusive [17] electron scattering experiments have been done for ^{16}O. By studying this nucleus we can therefore make a comparison with our previous results and also test the consistency of the description of the various experiments. Obviously the formalism could have been applied to study any other doubly closed shell nucleus.

4.1 Testing the direct knock-out model

Our model has been developed with the aim of providing a good description of the SRC correlations. Since the presence of collective phenomena has not been considered, the range of applicability of our model is limited to those kinematic situations where the effects of these phenomena can be neglected.

In our previous works the model has been applied in the quasi-elastic region [13, 14, 16, 17]. It has been verified in Ref. [44] that in this region collective excitations described in terms of continuum RPA are negligible and their effects become smaller with increasing momentum transfer. The modification of the IPM responses is produced by the Final State Interactions (FSI) between the emitted nucleon and the rest nucleus. Second RPA calculations [45] showed that, in the quasi-elastic region, the FSI effects can be accounted for by using an optical potential. The mean-field model implemented with optical potentials taken from nucleon-nucleus elastic scattering data is the approach

proposed by the Pavia group [26, 46] and successfully used to analyze the nucleon emission data.

In Ref. [15] our model was applied to study low-lying states excitations. Also in this case we excluded collective excitations and we studied data at large values of the momentum transfer, above 300 MeV/c.

Clearly, the electron scattering kinematics ensuring the dominance of the single particle excitations are not achievable with photons. Furthermore, in the literature it is well known that continuum RPA calculations successfully describe photon reactions even at energies above the giant resonance region [24]. The photon excitation of doubly closed shell nuclei has been widely studied with self-consistent continuum RPA with Skyrme interactions, first by the Bologna [47]-[49] and later by the Gent group [50]-[52]. For this reason we felt necessary to study the importance of collective excitation modes in photo-reactions.

Our study of the effects of collective excitations has been done by using the Fourier-Bessel Continuum RPA approach of Ref. [53] used in the past to investigate coincidence electron scattering processes in the giant resonance region [28, 29] and inclusive quasi-elastic responses [44]. This RPA approach is based upon the Landau-Migdal theory of finite Fermi systems. The ground state is described by a phenomenological mean field potential and the residual effective interaction is fixed to reproduce some general properties of the system.

In our case the single particle basis has been generated by a mean field potential of Woods-Saxon type. In our RPA calculations both bound and continuum single particle wave functions have been produced by the same real Woods-Saxon potential. As already discussed in the previous section, the parameters of the potential are those used in Ref. [8] for the FHNC calculation.

The residual interaction has the form

$$\begin{aligned} V(1,2) &= C_0 \left[f(r_{12}) + f'(r_{12}) \boldsymbol{\sigma}(1) \cdot \boldsymbol{\sigma}(2) \right. \\ &+ \left. g(r_{12}) \boldsymbol{\tau}(1) \cdot \boldsymbol{\tau}(2) + g'(r_{12}) \boldsymbol{\sigma}(1) \cdot \boldsymbol{\sigma}(2) \boldsymbol{\tau}(1) \cdot \boldsymbol{\tau}(2) \right] , \end{aligned} \tag{27}$$

where we have indicated with r_{12} the distance between the two interacting nucleons. In the above equation we used the traditional nomenclature to identify the various terms of the force. One should not confuse the $f(r_{12})$ in Eq. (27) with the correlation function in Eq. (22). We made calculations with two types of effective forces: a zero-range Landau-Migdal interaction and the finite range polarization potential of Ref. [54]. For the Landau-Migdal interaction the functions f, f', g, and g' are constants. The values of these parameters have been chosen as in Ref. [28] where it has been shown that they provide a reasonable description of the giant resonances and of the low-lying excited states. With this set of values we obtained the energy of the collective low-lying 3^- state at 6.40 MeV against the experimental value of 6.15 MeV.

One of the interesting features of the finite range polarization potential is the fact that it is built to take into account effectively the exchange terms. This fact is very important in our case, since our Fourier-Bessel RPA calculations do not consider these terms. We straightforwardly used the interaction as given in Ref. [54] and we obtained for the energy of the low-lying 3^- state the value of 6.65 MeV.

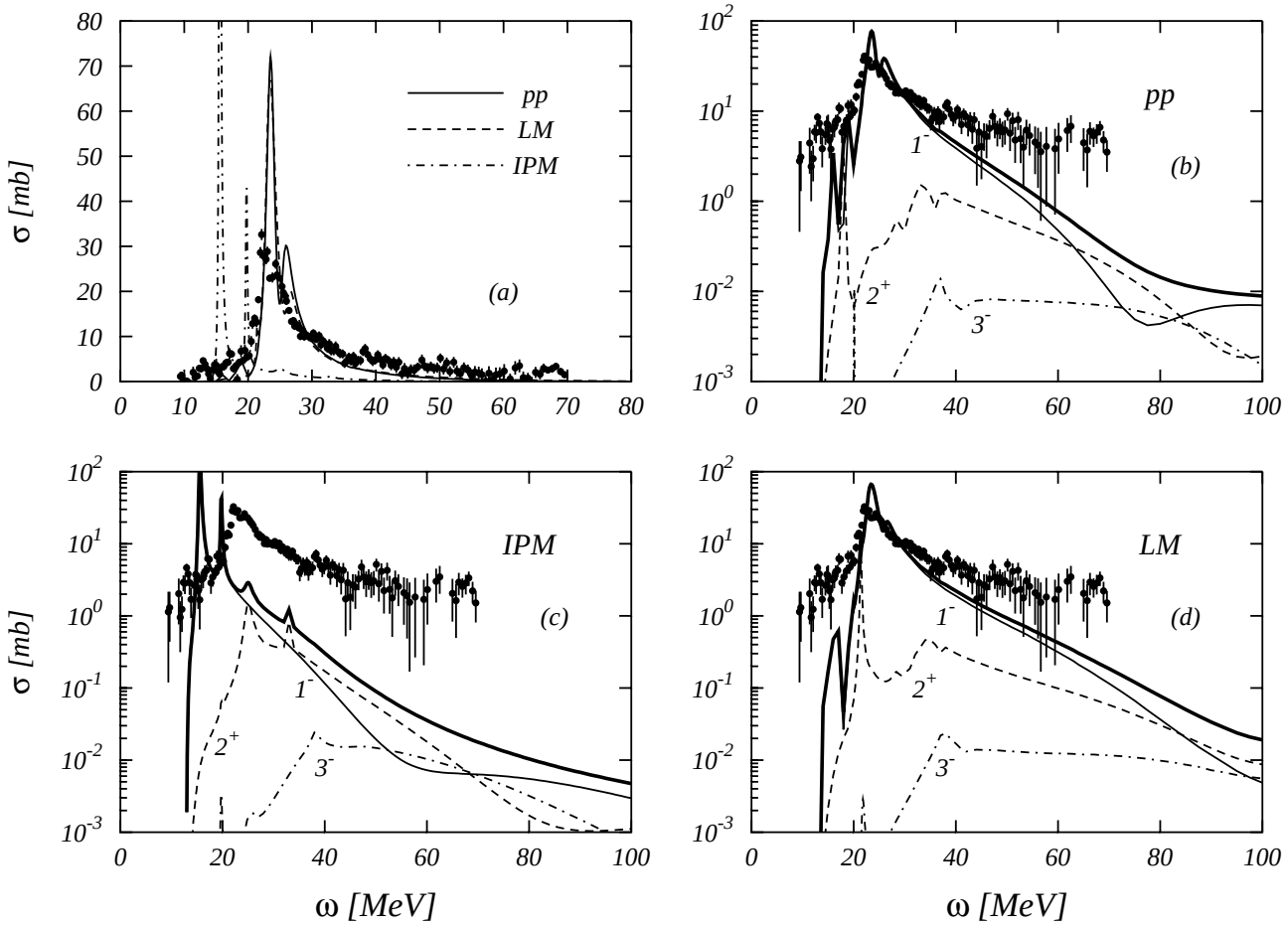

Figure 3: Total photoabsorption cross sections calculated in the IPM and with the continuum RPA by using the polarization potential (pp) and the Landau-Migdal (LM) residual interactions. In panels (b), (c) and (d) the contribution of the main electric multipoles is shown and the full thick line represents the total cross section. The data are from Ref. [55].

All the calculations we shall discuss in this subsection have been done by using OB currents only. In Fig. 3 we compare our results, obtained by considering all the excitation multipoles up to $J = 3$, with the total photoabsorption data of Ref. [55]. The panel (a) of the figure shows that while the RPA calculations are able to reproduce the centroid energy of the giant resonance, the IPM cannot do it. However, even in RPA results, the height of the peak is overestimated and the width underestimated. These facts are rather well known in the literature [56]. The deficiencies of the RPA have been widely investigated, and it seems that they can be cured by considering excitations beyond 1p-1h, like in the Second RPA [57] or in the phonon coupling scheme [58, 59].

Since we are interested in the region beyond the giant resonance, we emphasize the comparison between theory and experiment in the panels (b), (c) and (d) of Fig. 3 by using the logarithmic scale. In these three panels we show the contribution to the total cross sections of each electric multipole. The contribution of the magnetic multipoles is too small to appear in the figure. The three calculations show that the 1^- excitation is the

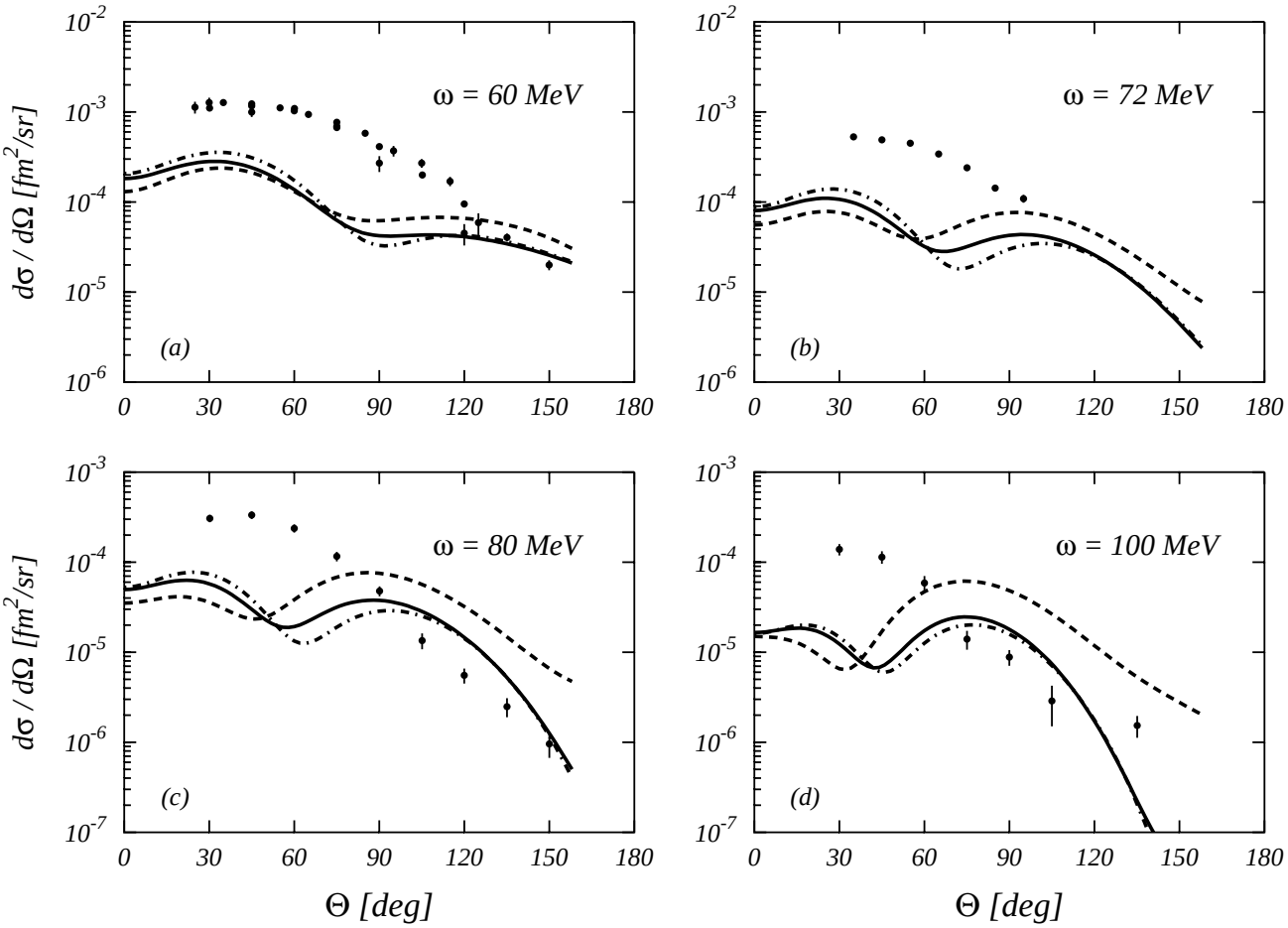

Figure 4: Angular distributions of the ^{16}O(γ,p$_0$)^{15}N reaction for various energies of the photon. The full lines show the RPA results obtained with the polarization potential, the dashed lines the RPA results obtained with Landau-Migdal interaction and the dashed-dotted line the IPM results. The data have been taken from Ref. [60] and also from [61, 62] in the panel (a).

dominant one in the giant resonance region, but with increasing energy the contribution of the 2^+, and that of the 3^-, becomes important. The relevance of the high multipolarity is related to the residual interaction. In the IPM the 2^+ cannot be neglected already at 40 MeV, while the dominance of the 1^- is extended at larger energies in the RPA calculations: 60 MeV for the polarization potential and 80 MeV for the LM interaction. This result is in agreement with the findings of Ref. [52]. The IPM results are, in the region above 40 MeV, one order of magnitude smaller than those obtained with the RPA. One should remark, however, that even the RPA calculations are below the data in the region of interest.

If the total photoabsorption cross section cannot be reproduced we have little hope to reproduce the exclusive cross section. Indeed the observation of Figs. 4 and 5 confirms this expectation. In these figures we compare the ^{16}O(γ,p$_0$)^{15}N and ^{16}O(γ,n$_0$)^{15}O data of Refs. [60]-[62] and [63] with our RPA and IPM calculations. All the curves underestimate the data, as we expected.

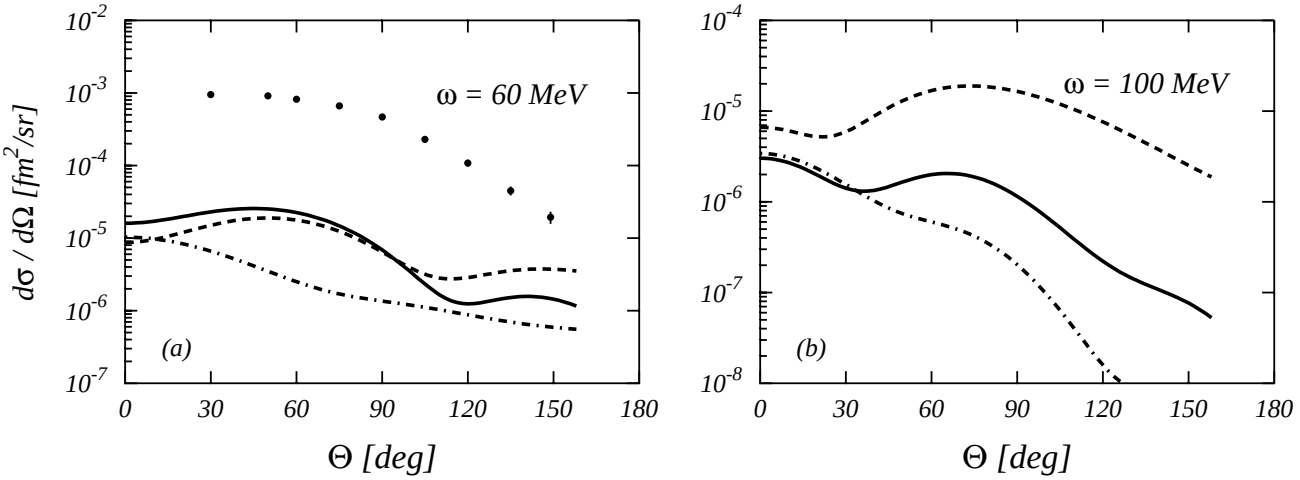

Figure 5: Angular distribution of the $^{16}O(\gamma,n_0)^{15}O$ reaction for two photon energies. The meaning of the lines is the same as in Fig. 4. The data are from Ref. [63].

In Fig. 4 the IPM and the RPA results obtained with the polarization potential are rather similar, while those obtained with the Landau-Migdal interaction differ more. This fact is consistent with the study done in the electron scattering case [44, 64]. The finite range interactions become weaker with increasing momentum, while contact interactions are constant in momentum space. For this reason the zero-range interaction, tuned to reproduce low-energy nuclear properties, overestimates the role of the RPA above the giant resonance region. The momentum behavior of finite-range interactions is more realistic than that of the zero-range forces, therefore in the estimate of the collective effects we refer to the results obtained with the polarization potential. These results indicate that the RPA effects become smaller with the increase of the photon energy. For proton emission at 100 MeV these effects are really negligible, and the cross section is essentially that of the IPM.

The situation for the neutron emission is rather different, as it is shown in Fig. 5. Here IPM and RPA results are very different. The photon couples to a neutron only through its magnetic moment and, only for the 1^- excitation to its effective charge [25]. In sect. 4.2 we shall show that, at the photon point, the magnetization current is much smaller than the convection one. For this reason the dominant mechanism ruling the neutron emission is not the direct knock-out, but a re-scattering process where the proton struck by the photon interacts with the neutron which is emitted. Continuum RPA calculations partially take into account these re-scattering phenomena, for this reason RPA neutron emission cross sections are much larger than the IPM cross sections. This increase is however not sufficient to obtain a reasonable description of the 60 MeV data of panel (a).

The fact that experimentally the neutron emission cross section is of the same order of magnitude of the proton emission cross section is an open problem deserving further investigation, but it is out of the scope of the present paper. Our RPA calculations were aimed to test the applicability of the direct knock-out model. From the results we have presented we may conclude that this model can be used to describe the proton photo-emission for energies above the giant resonance region. Henceforth we shall restrict our

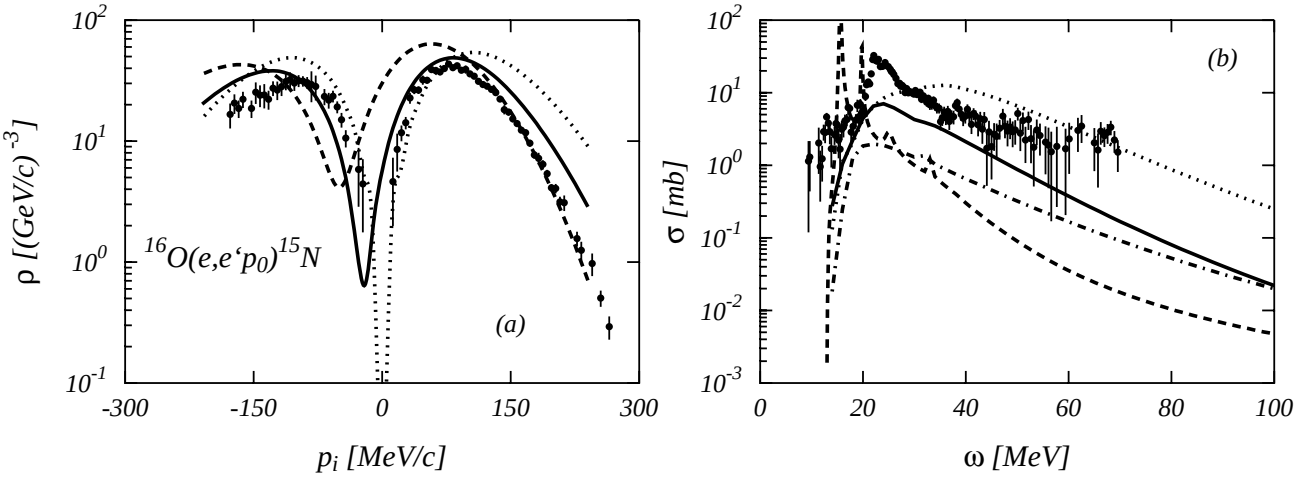

Figure 6: Panel (a): reduced ^{16}O(e,e'p$_0$)^{15}N cross section compared with the data of Ref. [68]. The dashed line has been obtained with the real mean-field potential. The full line corresponds to the calculation performed by using the optical potential of Ref. [67] for the particle states. The dotted line show the PWIA results. Panel (b): total photoabsorption cross section (data of Ref. [55]). The full, dashed and dotted lines have same meaning as those of panel (a). The dashed dotted line has been calculated considering the energy dependence of the optical potential.

investigation to this case.

Even though we restrict ourselves to the case of proton emission, where IPM and RPA results are very similar, the comparison with the experimental data shown in Fig. 4 indicates that some important physics effects are still missing. We have already mentioned the relevance of the FSI in the description of the quasi-elastic electron scattering data. In the calculation of the inclusive responses [16] we have treated the FSI using the folding model developed in Ref. [44]. In treating (e,e'p) reactions we chose the approach of the Pavia group [26, 46] which takes into account the FSI by describing the emitted nucleon as moving in an optical potential. We have adopted the same strategy also in the present work. In this type of calculations the single particle basis is not any more orthonormal since particle and hole wavefunctions are described by two different mean fields. This problem has been investigated in Refs. [65, 66] where it has been found that the effects of the non orthogonality of the basis are not important under in the kinematic conditions of interest.

In our calculations we used the optical potential of Schwandt *et al.* [67] which was adopted in the analysis of NIKHEF ^{16}O(e,e'p)^{15}N data [68]. In the panel (a) of Fig. 6 we show the reduced cross sections of the above reaction calculated with the real mean field potential (dashed line) and with the optical potential (full line). The improvement in the description of the data is evident, even though the theory is still above the experimental points. The dotted line show the result obtained by considering the wave function of the emitted particle to be a plane wave. This approximation is usually called Plane Wave Impulse Approximation (PWIA) [26].

In the panel (b) of the same figure we show the total photoabsorption cross section. The full, dashed and dotted lines have been obtained with the same inputs used for the analogous curves of panel (a). The results of this figure indicate that, above the giant resonance region, the cross section strongly depends on the mean–field potential describing the emitted particle. The cross section becomes smaller when the depth of the real part of this potential increases. The lowest cross section (dashed line) is obtained by using the purely real Woods-Saxon potential of Ref. [8] which is the deepest one among those we have used. As expected, the dotted line showing the PWIA results is above all, experimental data included. In between there are the results obtained with the Schwandt *et al.* potential. Specifically, the full line has been obtained with the parameters fixed to evaluate the (e,e'p) cross section of the panel (a). In this case the real part of the potential is shallower than that of the potential of Ref. [8]. The dashed-dotted line was calculated changing the parameters of the optical potential at each excitation energy, strictly following the parameterization given in Ref. [67]. The real part of the potential becomes shallower with increasing energy. This effect is present in the phenomenological optical potentials fixed to fit elastic nucleon-nucleus scattering data, like the potential we are using, and also in the optical potentials evaluated in microscopic many-body theories [69, 70].

The angular distributions of the $^{16}O(\gamma,p_0)^{15}N$ cross sections calculated for various photon energies by using different potentials are compared in Fig. 7 with the experimental data of Refs. [60]-[62, 71]. The agreement between data and the cross section obtained by using the optical potential is remarkable. Despite the differences in the angular distributions, the order of magnitude of the cross sections is correct, contrary to the results obtained with the real mean field (dashed curves), always smaller than the data, and those obtained in PWIA (dotted curves), always larger than the data.

We should mention at this point that the RPA calculations of Refs. [48, 52], done with Skyrme type interactions, reproduce both proton and neutron emission data better than our RPA results. This indicates that in some parameterization of this interaction, the FSI effects are effectively considered. However the results are extremely sensitive to the choice of the parameters, as it is shown in Refs. [48, 52] where results obtained with different interactions are compared.

Henceforth we shall investigate the proton emission cross sections by using the direct knock-out model (no RPA) with the energy dependent optical potential of Schwandt *et al.* [67].

4.2 The electromagnetic currents

The effects of the SRC we aim to disentangle, are certainly small in comparison with the total size of the cross section. It is therefore mandatory to control all the approximations of our model, to be sure that the size of the effects we found do not fall within the uncertainty of our theoretical hypotheses. In this subsection we discuss those hypotheses related to the treatment of the electromagnetic currents.

The usual treatment of the photonuclear processes is based on the Long Wave Approx-

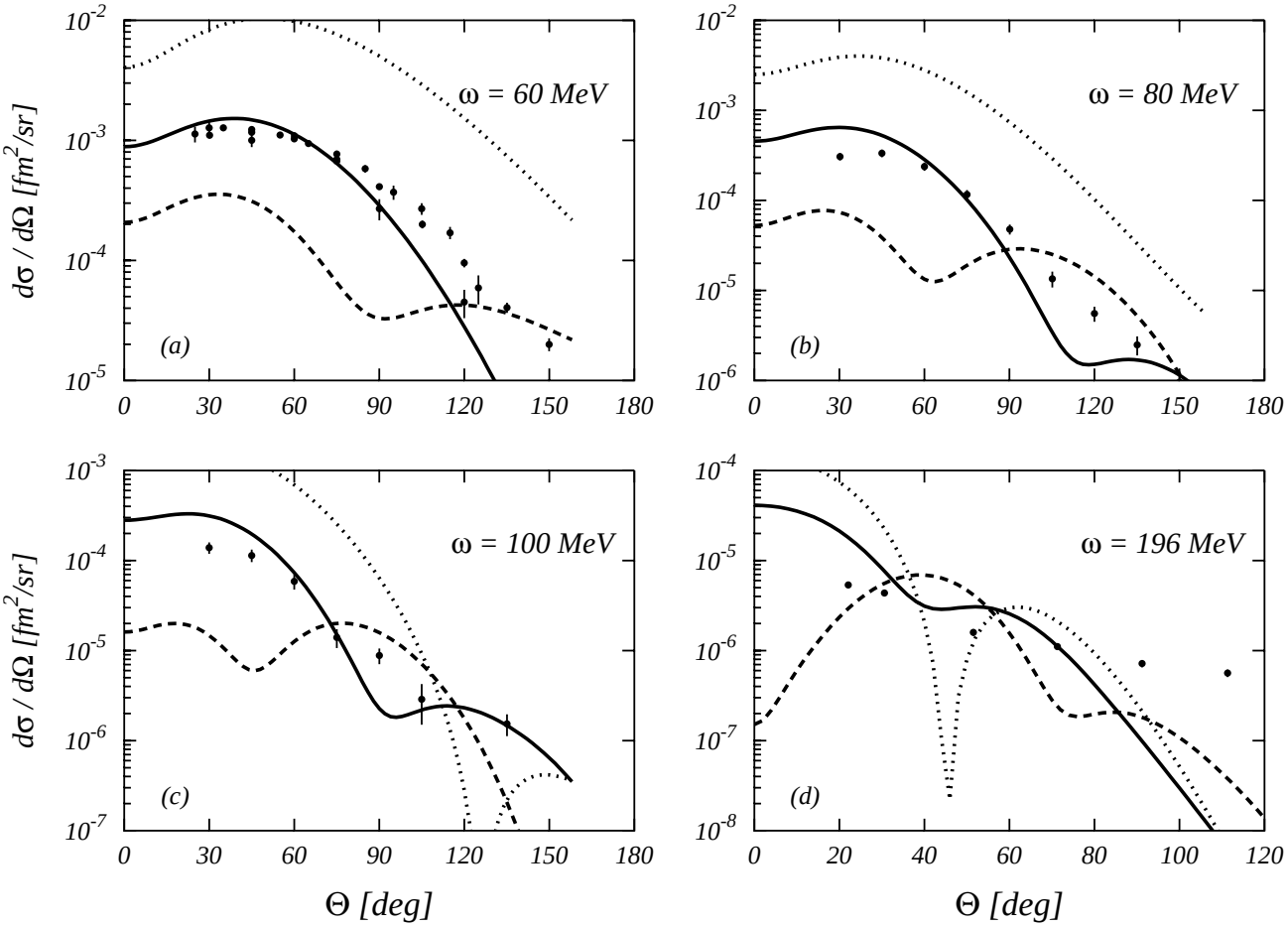

Figure 7: Cross sections of the $^{16}O(\gamma,p_0)^{15}N$ reaction for various energies of the photon. The full lines have been obtained using, for the particle states, the energy dependent optical potential of Ref. [67], the dashed lines with the real potential potential of Ref. [8] also used for the hole states, and the dotted lines have been obtained in PWIA. The 60, 80 and 100 MeV data are those already shown in Fig. 4. The 196 MeV data are from Ref. [71].

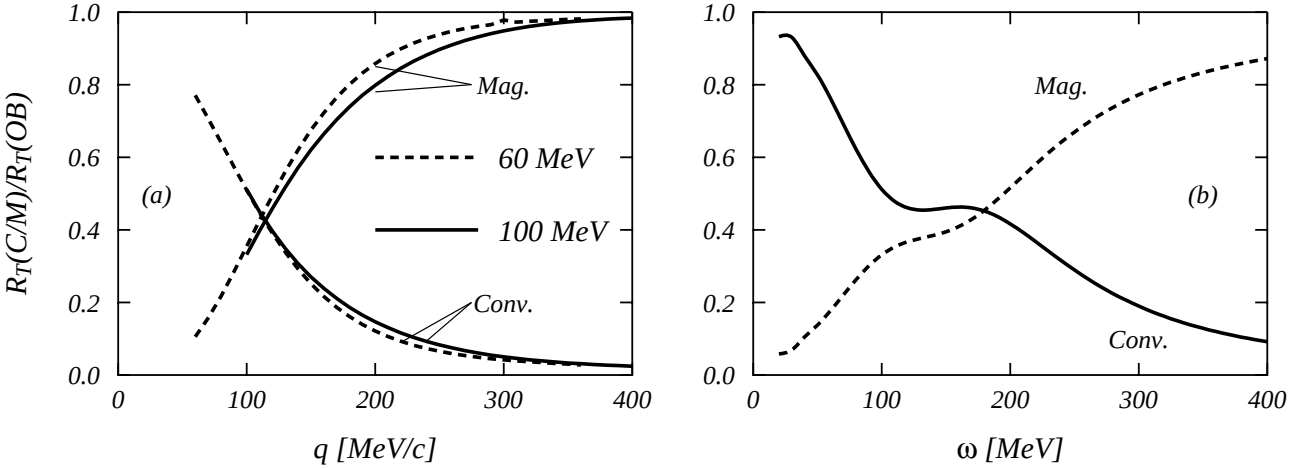

Figure 8: Ratio between transverse responses calculated by using only convection or magnetization current and the full OB current response. In the panel (a) the excitation energies have been fixed and the momentum transfer q has changed. In the panel (b) the ratios have been calculated at the photon point for various values of the excitation energy.

imation (LWA) and on the Siegert's theorem which allows one to substitute the convection current with the charge density operator [25]. We have investigated the validity of these approximations in the energy region above the giant resonance and our conclusions are analogous to those obtained in Refs. [50, 52]. The two main points are that, in this region, the LWA starts to lose its validity and that multipole excitations other than the 1^- become important. For these reasons in our calculations we used the explicit expression of the convection current operator and in the evaluation of the (γ,p) cross section we inserted all the electric and magnetic multipoles up to J=12 (see Eq. (3)). This last requirement was necessary to ensure the numerical stability at large values of the emission angle, even at the highest photon energies investigated.

We have studied the relevance of the OB magnetization current, Eq. (11), usually neglected in the study of photo-nuclear reactions [24, 25, 49, 52]. The ratios between the transverse responses, Eq. (1), calculated using only the convection or the magnetization current and the responses obtained with the full OB current are shown in Fig. 8.

The panel (a) of the figure show that at the photon point ($q = \omega$) the contribution of the convection current is larger than that of the magnetization current. With the increase of the momentum transfer, the relative importance of the two currents is interchanged. In the quasi-elastic regime the magnetic current dominates as it is well known [21]. Even at the photon point the relative importance of the magnetization current increases with increasing energy. This trend is shown in the panel (b) of the figure, where the relative ratios calculated at the photon points are given as a function of the excitation energy.

The effects of the MEC on the photonuclear reactions are estimated to be more important than in electron scattering. This information comes from indirect evaluation of MEC in RPA calculations based on the charge-current continuity equation [49, 52, 72] and also from their explicit calculation as it is done in Refs. [73]-[76].

In order to discuss the effects of the MEC we show in Fig. 9 normalized differences

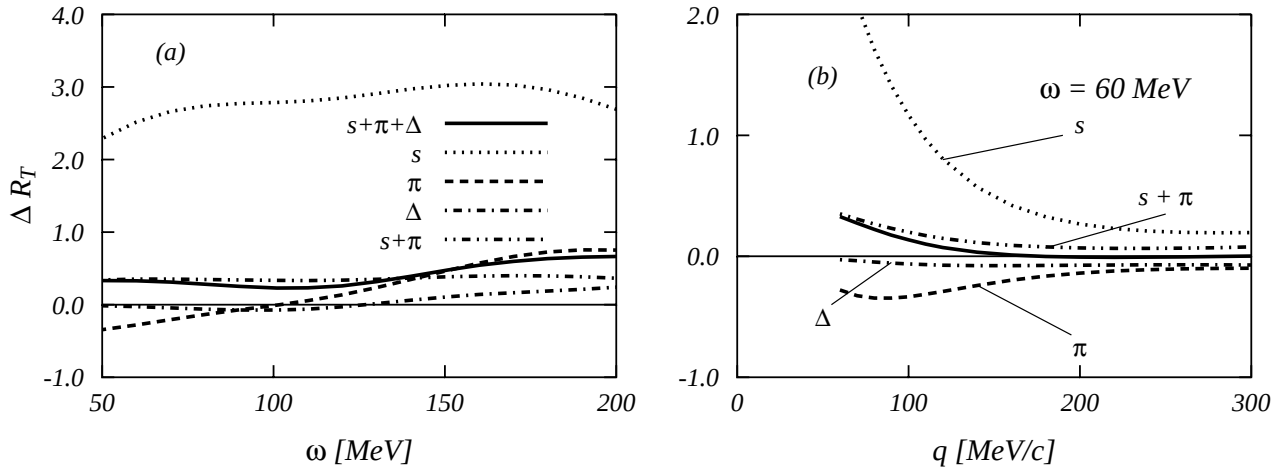

Figure 9: Normalized differences, Eq. (28), obtained by adding to the OB currents the various MEC terms indicated in the figure. The normalized differences have been calculated at the photon point (panel (a)) and at fixed excitation energy $\omega = 60$ MeV as a function of the momentum transfer q (panel (b)). The labels indicates the MEC included: (s) the seagull, (π) the pionic, (Δ) the Δ current, and (s + π) both seagull and pionic currents. The full lines have been obtained by considering all the currents.

defined as

$$\Delta R_T(q,\omega) = \frac{R_T(OB+MEC) - R_T(OB)}{R_T(OB)}\,, \tag{28}$$

where we have indicated with $OB + MEC$ the responses obtained by adding the various MEC terms to the OB currents. In the panel (a) of the figure the normalized differences calculated at the photon point are shown as a function of the excitation energy. In the panel (b) as a function of the momentum transfer for fixed excitation energy $\omega = 60$ MeV.

The results presented in Fig. 9 shows that the inclusion of the seagull term only, as it is done for example in Refs. [75, 76], largely overestimates the role of the MEC. The pionic current alone reduces the OB response at energies smaller than 100 MeV, and it slightly increases it at larger values. The presence of destructive interference between seagull and pionic currents is well known in the studies of the quasi-elastic peak [22, 36]. The dashed doubly dotted line of the figure shows the result obtained by including both currents.

The contribution of the Δ current is relatively small. We should remark that we consider only the virtual excitation of Δ, and do not include the pion production channel which implies the real delta excitation. This channel is open above ω=140 MeV.

Panel (b) show that at the photon point the contribution of the seagull term is relatively larger than at higher q values. The pionic term reduces the OB response for all q values. The interference between these two terms is the dominant contribution since the Δ current is negligible. The full line shows that the inclusion of all the MEC diagrams produces relatively small variations on the OB currents. It is worth to notice that the relative difference becomes smaller with increasing momentum transfer. The photon point is the place where the MEC effects are largest, on a relative scale.

In Fig. 10 we compare the angular distributions of the ^{16}O(γ,p$_0$)^{15}N cross sections

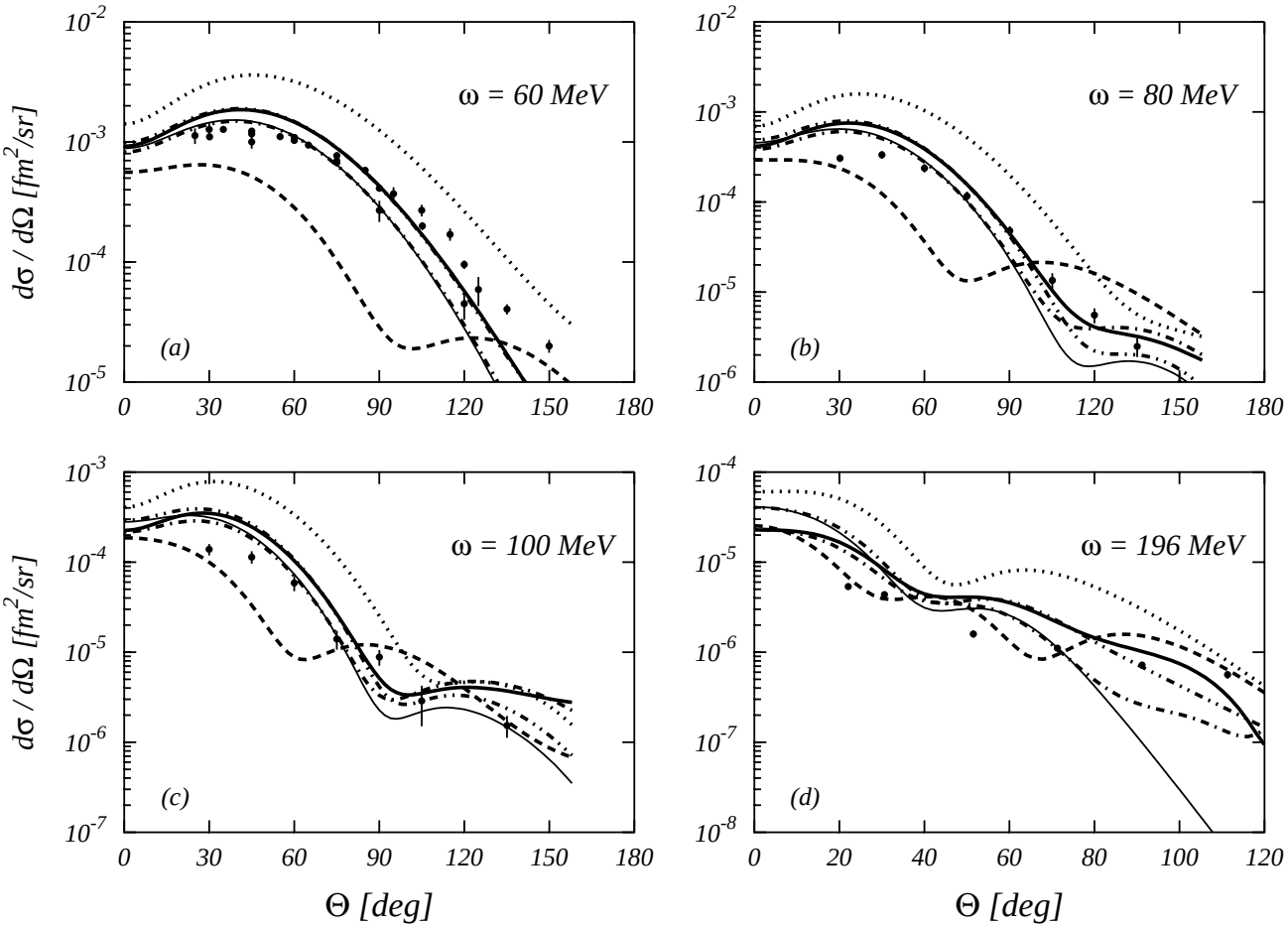

Figure 10: Angular distribution of the $^{16}O(\gamma,p_0)^{15}N$ cross section for various energies of the photon. The thin full lines show the OB results, the other lines have been obtained by adding the various terms of the MEC: dotted lines, OB+seagull, dashed lines, OB+pionic, dashed-dotted, OB+Δ, dashed-doubly-dotted, OB+seagull+pionic. The thick full lines show the results obtained once all the currents are included. Data as in Fig. 7.

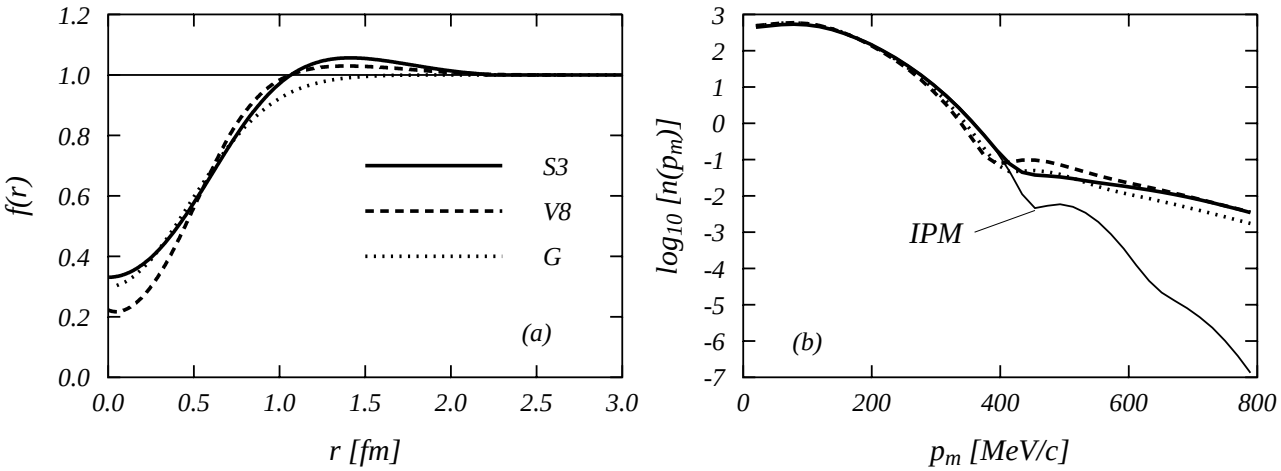

Figure 11: Left panel: correlation functions considered in our calculations. Right panels: momentum distributions calculated with the correlations of the left panel.

calculated for various photon energies. The calculations have been done with the optical potential and the thin full lines represent the results obtained with the OB currents only. The other lines have been obtained by adding the various MEC terms. The contribution of the seagull current (dotted lines) noticeably increases the cross section, but the effect of the pionic current (dashed lines) goes in the opposite direction. When both currents are considered (dashed-doubly dotted lines), the results are only slightly above the OB ones. The excitation of the virtual Δ (dashed-dotted lines) is not important but at high values of Θ and at high photon energies. The total results (thick full lines) are slightly above the OB ones, the differences become larger at high values of Θ.

The results obtained with the OB currents only (thin full lines) steeply decrease with increasing Θ. At high Θ values the inclusion of seagull and pionic currents pushes up the cross section by an order of magnitude.

4.3 The short-range correlations

We have investigated the effects of the SRC by evaluating the (γ, p) cross sections with different correlation functions. The hole wave functions and the correlation functions have been fixed in Ref. [8] to minimize the nuclear hamiltonian calculated with the S3 interaction of Afnan and Tang [41]. We used the two types of correlation function selected in Ref. [8]: a first one obtained with the Euler procedure, labelled S3 in the panel (a) of Fig. 11, and a second one of gaussian type, labelled G. For sake of comparison we also used the scalar part of the state dependent correlation function taken from [9] where the hamiltonian expectation value has been calculated with a more realistic interaction: the V8' Argonne interaction [5].

In the panel (b) of Fig. 11 the ground state momentum distributions calculated with the first order model of Ref. [3] are shown for the three different correlations. The behavior of the various results show the well known increase at high momentum values with respect to the IPM result [1]-[4]. There are not striking differences between the

momentum distributions obtained with the various correlation functions.

Since the novelty of our approach is the inclusion of the three point diagrams we have studied the importance of these terms. In Fig. 12 we show the normalized difference of Eq. (28) evaluated by adding to the OB terms the correlated two- and three-point diagrams instead of the MEC. The full lines have been obtained by considering all the diagrams of Fig. 2 and the dashed lines by adding to the IPM response the two-point diagrams only.

These results agree with the findings of Refs. [16] and [17] in the (e,e') and (e,e'p) reactions. The effect of the two-point diagrams, whatever it is, is lowered by the inclusion of the three point terms. It is interesting to notice that the effect of the S3 correlation is smaller than that of the other two correlations and it has opposite sign.

The angular distributions of the ^{16}O(γ,p$_0$)^{15}N cross sections calculated for different photon energies are shown in Fig. 13. The thin full lines show the pure IPM results. The thicker full, dashed and dotted lines have been obtained by including the contribution of the S3, V8 and gaussian correlations respectively. Also in this case the three correlations produce rather different effects.

The sensitivity of the results to the correlation is larger than in the case of electron scattering. We have investigated the source of this relatively high sensitivity by calculating the (e,e') electromagnetic responses at fixed excitation energy (ω=100 MeV) for various values of the momentum transfer. The results of these calculations are shown in Fig. 14. All the results shown in the left panels have been obtained by using the S3 correlation while those of the right panels with the gaussian correlation. The (a) and (f) panels show the longitudinal responses, not present in reactions with real photons. The full lines are the IPM responses and the dashed lines have been obtained by adding the correlations. Referring to Fig. 2, the full lines have been obtained using only the diagram 1.1 and the dashed lines with all the diagrams of the figure. In addition to these lines we show the responses calculated without the OB terms. This means that we used all the diagrams labelled 2 and 3 in Fig. 2 and we eliminated the contribution of the 1.1 diagram. The results of these calculations are shown by the dotted lines. The analogous results for the transverse responses are shown in the panels (c) and (h) of the figure. To emphasize the difference between the various responses, in the panels (b), (d), (g) and (i) we show the normalized differences.

As expected, for all the momentum transfer values calculated, the OB responses are orders of magnitude larger than the responses obtained only with the correlation terms. Also the qualitative behavior of the responses as a function of q is quite different. While the OB responses increase by more than two order of magnitude with increasing q the change of the correlated responses is much more limited. The consequence of this fact is that, relatively speaking, at the photon point IPM and correlated responses are closer in magnitude than at higher q. For this reason the photon cross sections are relatively more sensitive to the SRC than the electron scattering processes. The comparison between the normalized differences, shown in the (b), (d), (g) and (i) panels, is a measure of the importance of the interference effects between OB and correlation transition amplitudes. As expected the most important part of the correlation effects is due to these interference

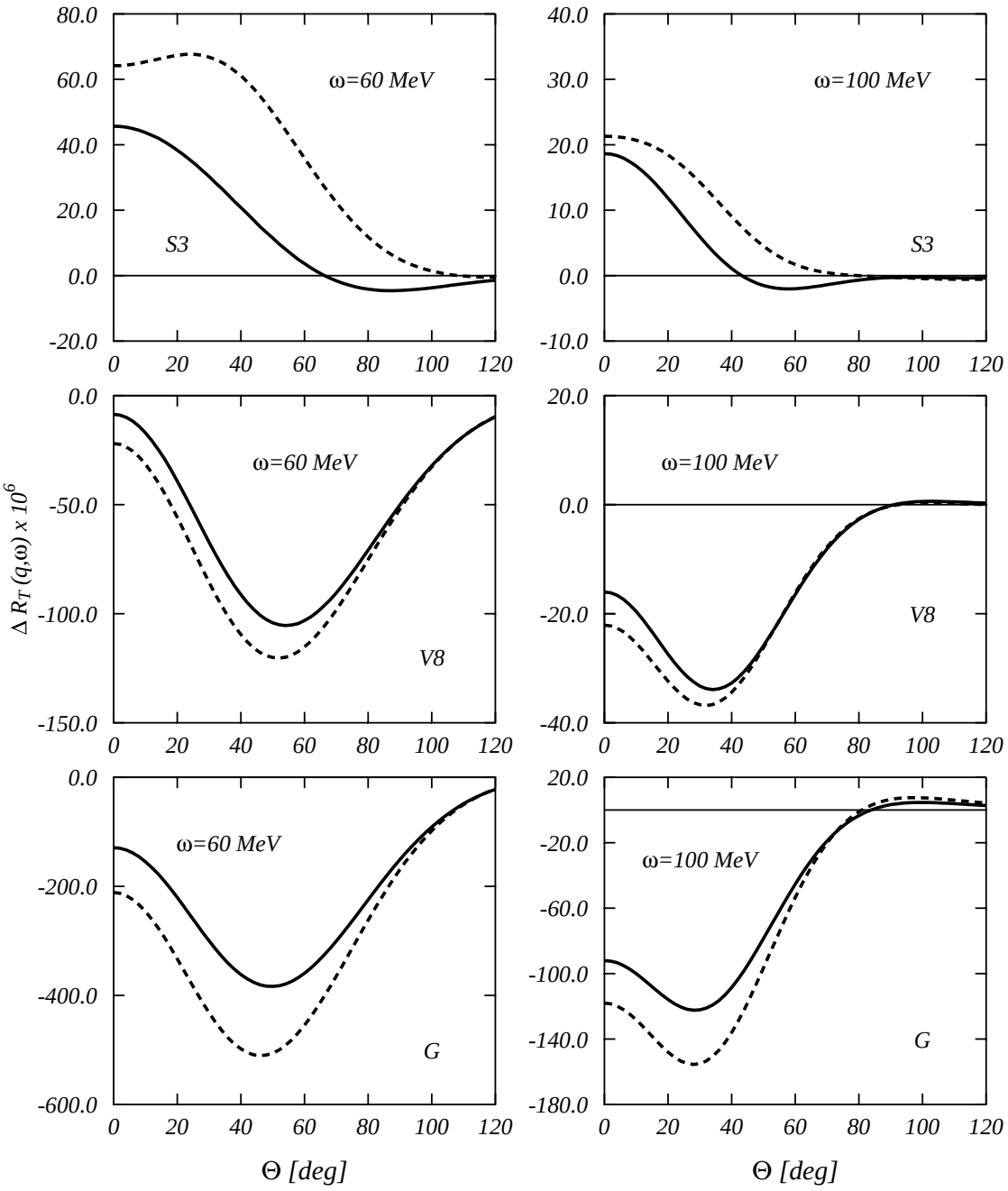

Figure 12: Normalized difference between correlated and uncorrelated responses for photon energies of 60 (left panels) and 100 (right panels) MeV. The dashed lines have been calculated with 2 point diagrams only, the full lines with both 2 and 3 point diagrams. The upper, medium and lower panels correspond to calculations performed with the S3, V8 and gaussian correlations, respectively.

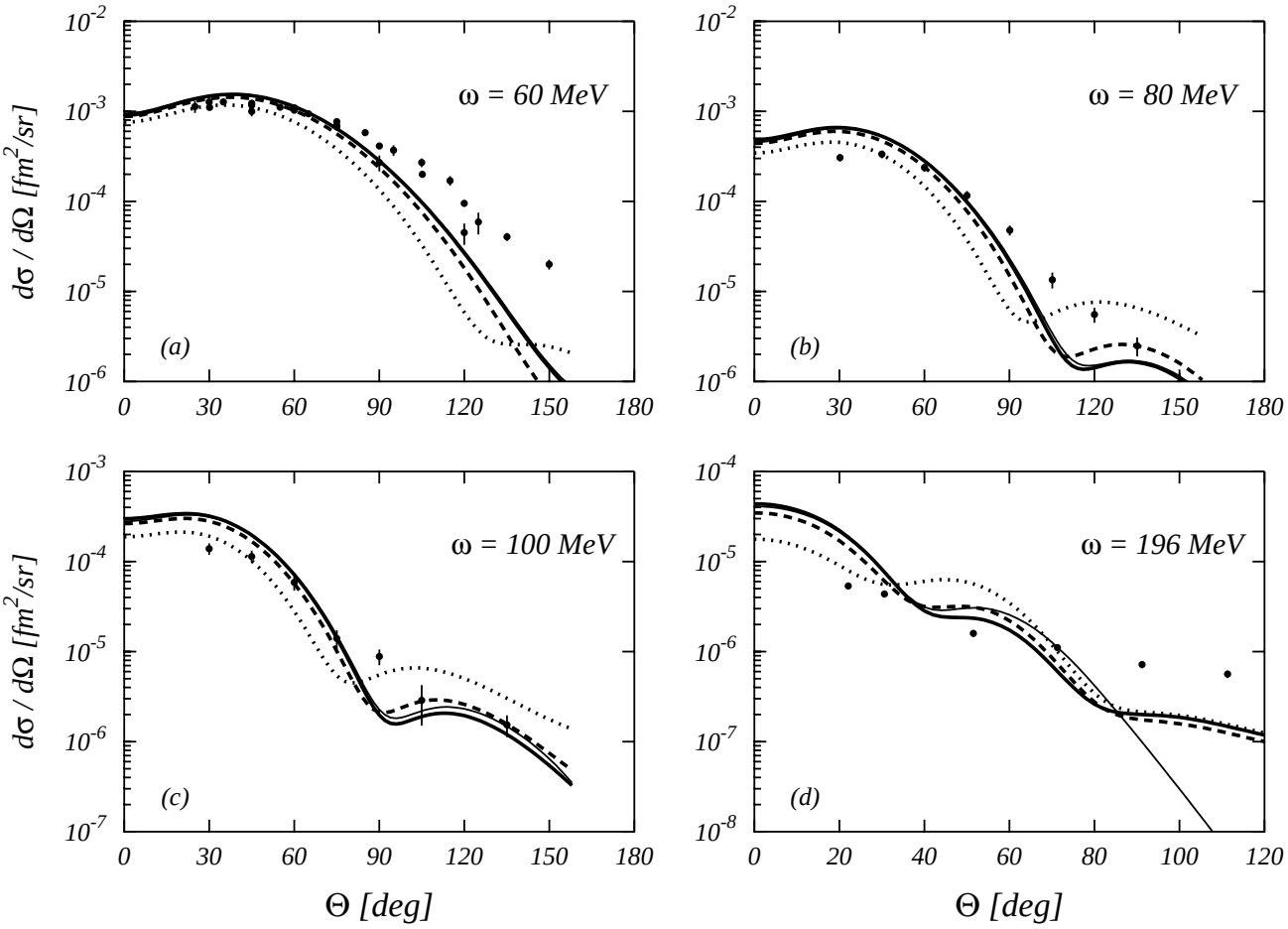

Figure 13: Angular distributions calculated with the inclusion of the SRC. The thin full lines are the IPM results, the thick full lines show the results obtained with the S3 correlation, the dashed lines with the V8 correlation function and the dotted lines with the gaussian correlation function.

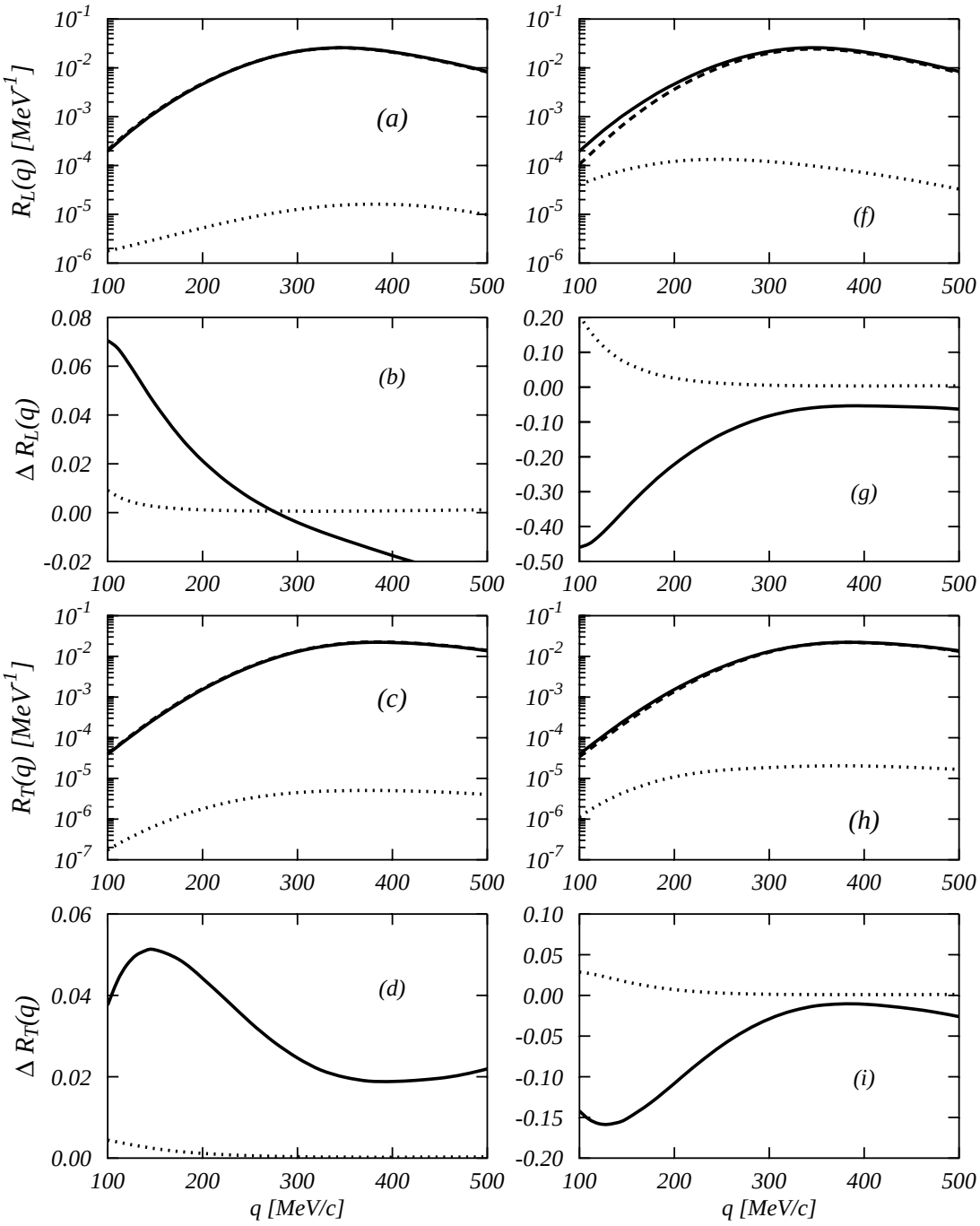

Figure 14: Inclusive responses and normalized ratios (see text) as a function of the momentum transfer at $\omega = 100$ MeV. Left panels refer to the S3 correlation; right ones to the gaussian correlations. The (a), (b), (f) and (g) panels correspond to the longitudinal response (not present in photonuclear processes) and the other ones to the transverse response. The full lines of panels (a), (c), (f) and (h) are the OB responses, the dashed ones the OB+correlations responses and the dotted lines the responses obtained only with the correlation terms. The full lines of panels (b), (d), (g) and (i) show the difference between OB and OB+correlation responses normalized to the OB response. The dotted lines the ratio between the responses obtained only with the correlation terms and the OB responses.

terms.

The observation of the angular distributions of Fig. 13 shows that at high values of the photon energy the correlation effects show up at large scattering angle. The IPM cross sections are almost overlapped to the thick full lines in Fig. 13. At 196 MeV the IPM cross sections show a fast decrease for large nucleon emission angles while the correlated cross sections indicates a less rapid fall. This behavior remember that of the momentum distribution of Fig. 11. In effect, by transforming the value of the emission angle Θ in the value of the momentum of the target nucleon p_i, it is possible to verify that the values of p_i probed go from 400 to 700 MeV/c. This is the interval where the correlated nucleon momentum distributions start to differ from that obtained with the IPM.

4.4 Comparison with data

The results we have so far obtained are summarized in the figures 15 and 16 to discuss their comparison with the data. The thin full lines have been calculated within the simple IPM by using OB currents only. The dotted lines show the results obtained by adding the S3 SRC obtained with the Euler procedure. The inclusion of the MEC produces the dashed lines. Finally the thick full lines have been obtained by including both SRC and MEC. Our calculations overestimate the data at small emission angles. This is evident in Fig. 15 and in Fig. 16 at ω=196 MeV where more data are available. The shape of the data at high energy values is reproduced only because of the inclusion of SRC and MEC. It is evident that the MEC contributions are larger than those of the SRC.

The energy dependence of the ^{16}O(γ,p$_0$)^{15}N cross section for fixed values of the emission angle is shown in Fig. 17. The meaning of the lines is the same as in Fig. 15. For Θ=45^0 our calculations show an almost perfect exponential decay. On the other hand the data are not so perfectly aligned. The discrepancy between our calculations and the data is more evident between 50 and 100 MeV. The shapes of the data and of our results for Θ=90^0 are characterized by two different trends: an exponential decay up to 100 MeV and an almost flat behavior at higher energies. This high energy tail is dominated by the MEC. We also observe that for $\omega > 100$ MeV the SRC effect consists in a reduction of the cross section.

In Fig. 18 we compare the results of our calculations with the data relative to the emission of the proton from the 1p$_{3/2}$ level [62]. The meaning of the various lines is the same as in Fig. 15. Also in this case our calculations slightly overestimate the data at small emission angles and underestimate them at larger angles. The SRC reduce the cross section while MEC increase it.

In all the calculations presented so far we did not make use of spectroscopic factors, a common practice in the analysis of (e,e'p) data. We fixed the spectroscopic factor as a reduction factor required by our ^{16}O(e,e'p$_0$)^{15}N results in order to reproduce the NIKHEF data of Ref. [68]. The comparison between our theory and the data is shown in the panel (a) of Fig. 19. From this comparison we obtained a spectroscopic factor of 0.8, as in Ref. [17].

In the panel (b) of Fig. 19 we compare the results of our calculations, including the

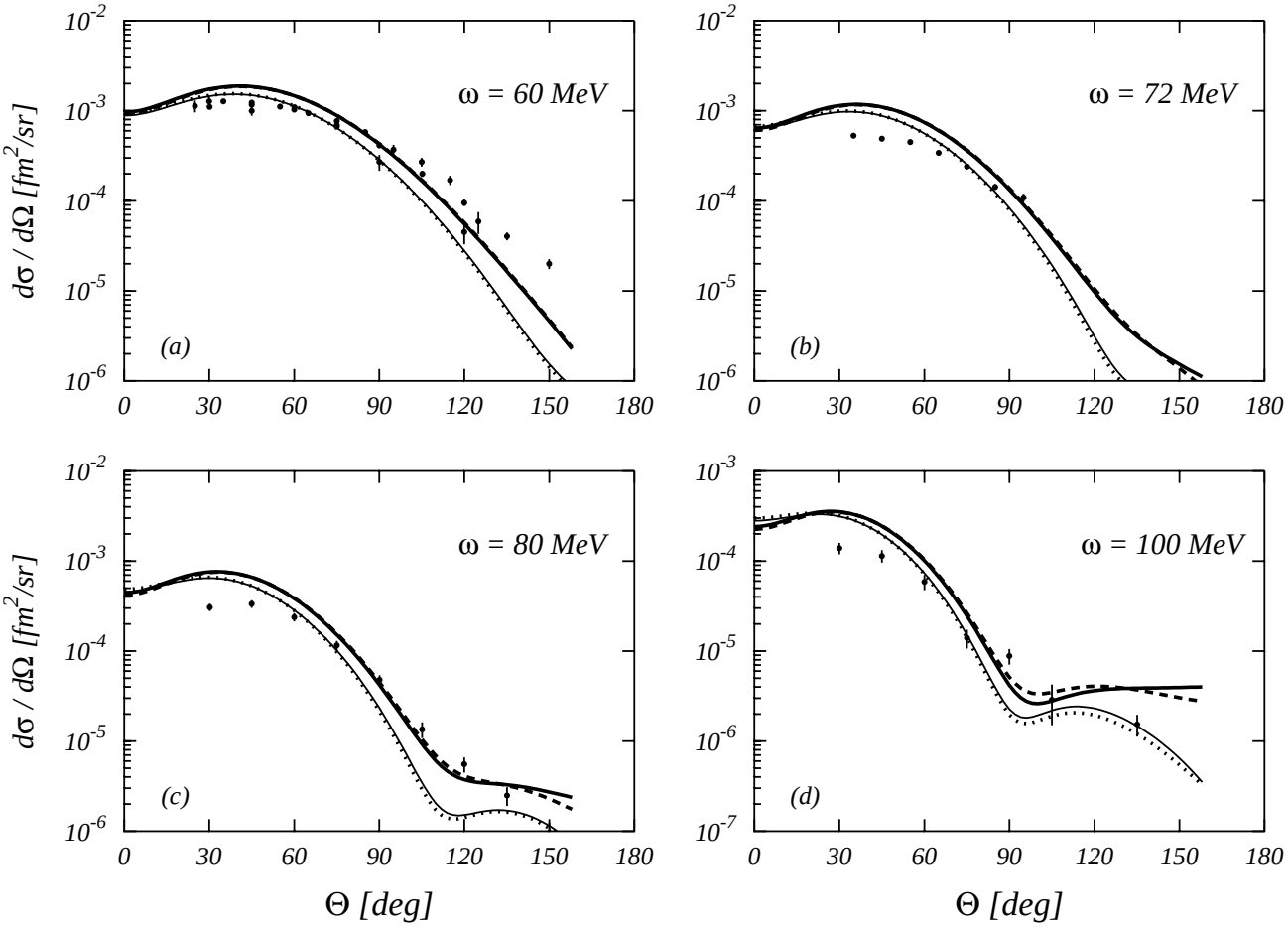

Figure 15: Angular distributions of the $^{16}O(\gamma,p_0)^{15}N$ cross section. The thin full lines have been calculated in the IPM by using OB currents only. The dotted lines include the effects of the S3 correlation. The dashed lines the MEC and the thick full lines all the effects. Data are from Refs. [60, 61, 62].

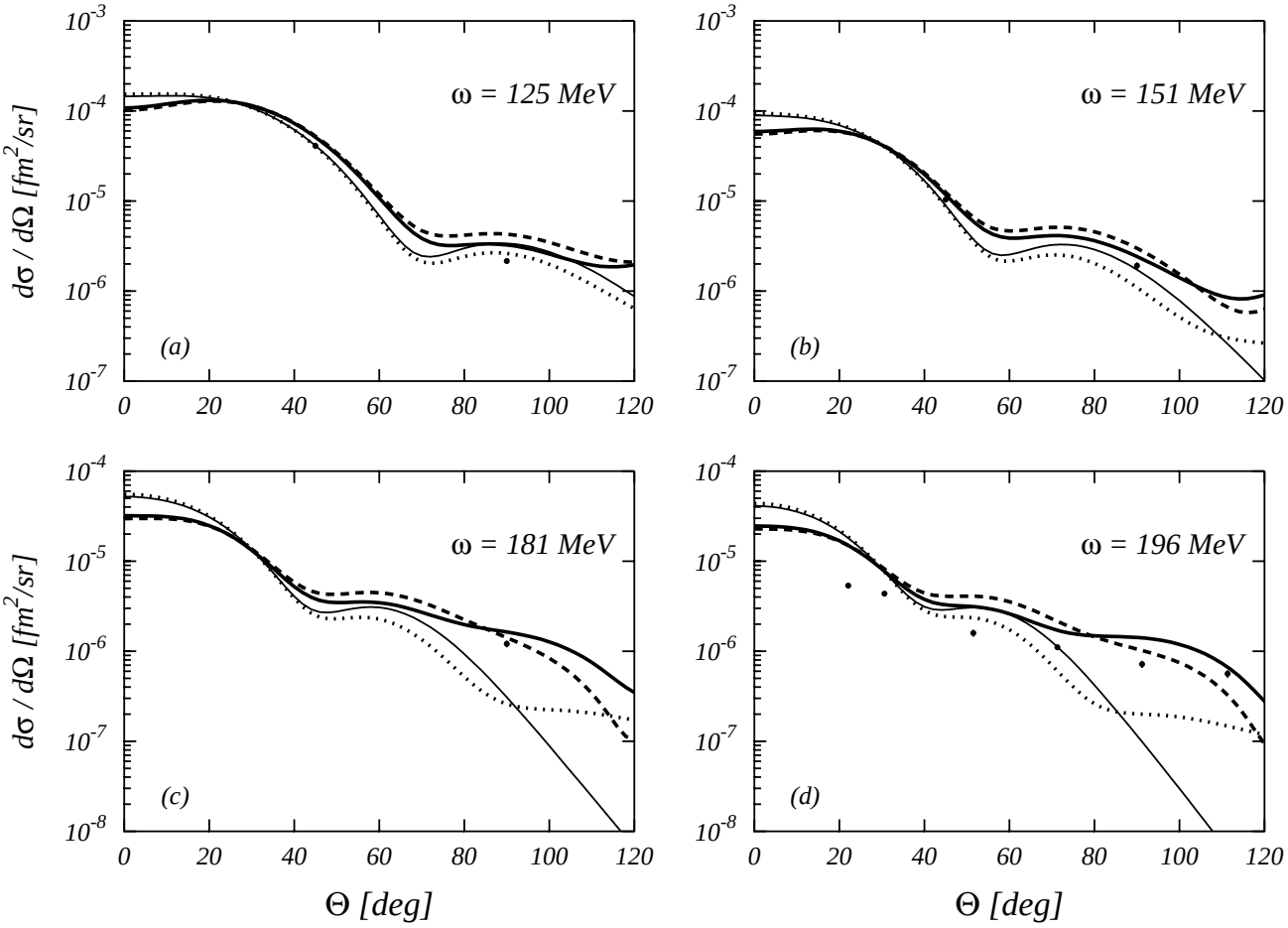

Figure 16: The same as in Fig. 15 for energies above 100 MeV. The data at 126, 151 and 180 MeV are from Ref. [77] and those at 196 MeV from Ref. [71].

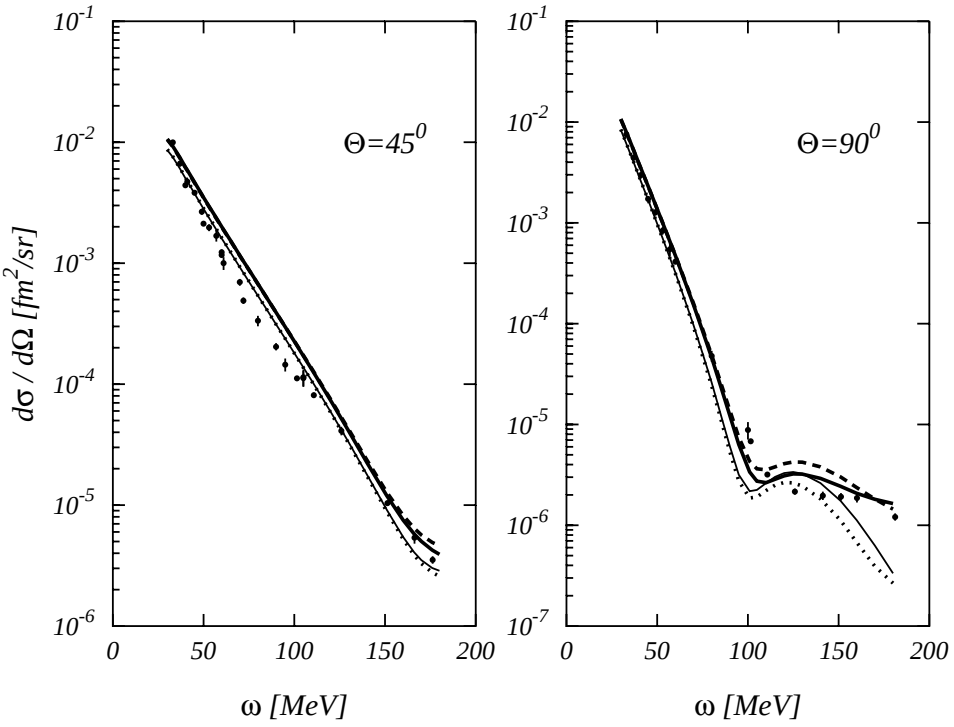

Figure 17: Energy dependence of the $^{16}O(\gamma,p_0)^{15}N$ cross section for various proton emission angles. Like in the previous figures, the thin full lines have been obtained with the IPM model, the dotted ones by adding the SRC, the dashed ones with the MEC and the full thick lines show the total results. Data are from [60, 61, 62, 77].

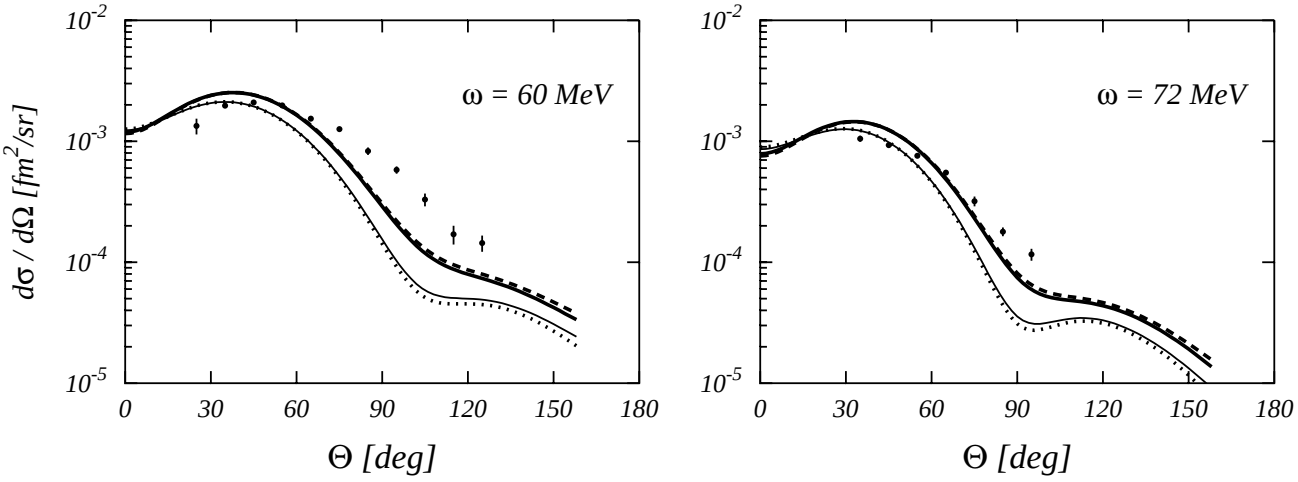

Figure 18: Angular distributions for the emission of a proton from the $1p_{3/2}$ level. The meaning of the lines is the same as in Fig. 15. Data are from Ref. [62].

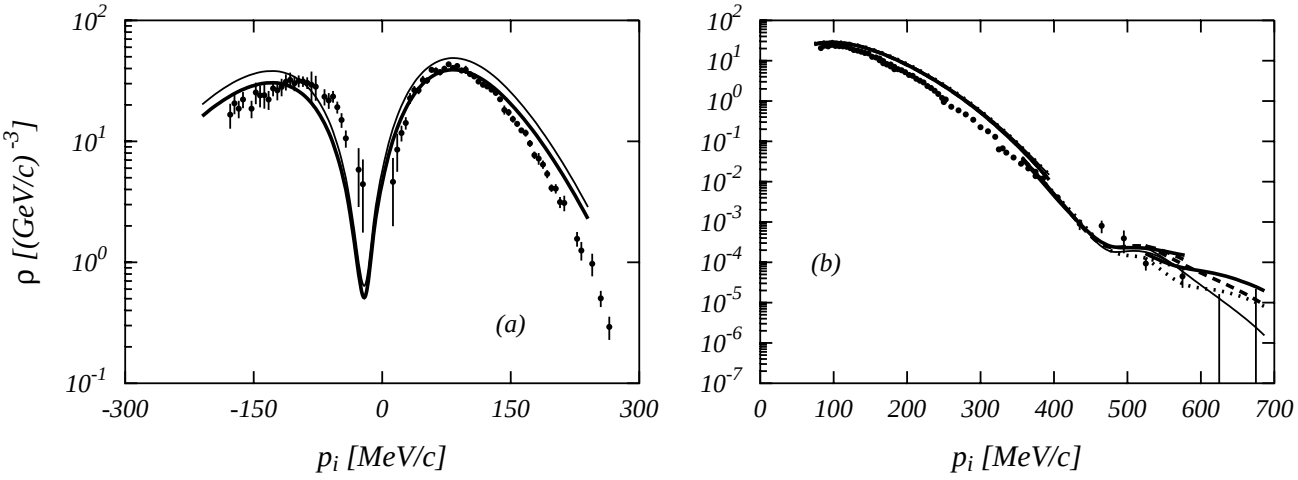

Figure 19: ^{16}O(e,e'p$_0$)^{15}N cross sections from NIKHEF [68], panel (a), and Mainz [78], panel (b), kinematics. In panel (a) the thin line represent the bare calculation while the full line has been multiplied by the spectroscopic factor of 0.8. All the curves of the panel (b) are multiplied by the spectroscopic factor. The meaning of the lines in this panel is the same as in Fig. 15.

spectroscopic factor, with the (e,e'p) data taken at Mainz [78]. The data at low p_i value are rather well reproduced, as it was expected because of the fit of the NIKHEF data covering the same range of p_i. From 200 to 300 MeV/c the theory overestimates the data, but theory and experiment have again a reasonable agreement at higher values of p_i. Also in this case the need of SRC and MEC to enhance the high momentum tail is evident.

Using the spectroscopic factor value of 0.8 we compare again the results of our calculations with the (γ,p$_0$) data in Fig. 20. In this figure the dashed lines represent the IPM results and the full lines the results of the calculations when SRC and MEC are included. The agreement with the data has certainly improved with respect to the results shown in Figs. 15 and 16. The inclusion of both MEC and SRC is necessary to obtain the correct shape of the data.

5 SUMMARY AND CONCLUSIONS

We have investigated the photonuclear cross section above the giant resonance region with the model presented in Ref. [16], which considers the contribution of the SRC at the first order in the correlation line. The application of our model has been focused on the ^{16}O nucleus.

We first studied the importance of the collective nuclear excitations in the energy region above the giant resonance. This has been done by calculating the total photoabsorption cross sections with the Fourier-Bessel continuum RPA approach of Refs. [28, 53]. We have used two different residual interactions, a zero range Landau–Migdal interaction and the finite range polarization potential of Ref. [54]. The results obtained did not differ very much, and showed that, while the position of the giant resonance is rather well reproduced, its width is too narrow. All our continuum RPA calculations above

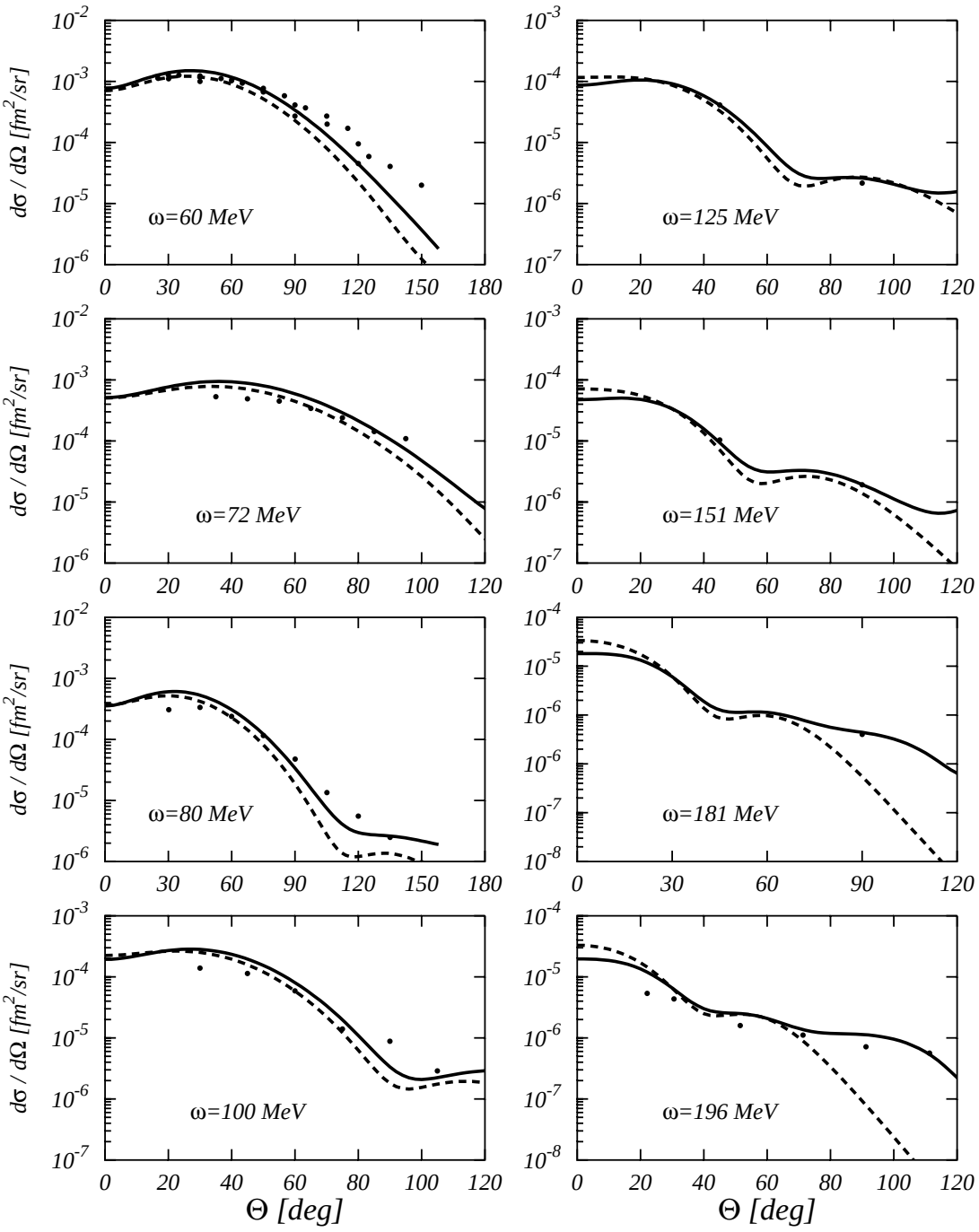

Figure 20: $^{16}O(\gamma,p_0)^{15}N$ cross sections for various values of the photon energies. All the curves have been multiplied by the spectroscopic factor of 0.8. The dashed lines show the IPM results with OB currents only and the full lines the results obtained by including both SRC and MEC. Data as in Fig. 13.

the giant resonance region underestimate the experimental total photo-absorption cross section. The IPM produces results which are more than one order of magnitude smaller than those of the RPA. The comparison with the (γ,p) angular distributions for photon energies above 60 MeV is very unsatisfactory.

We found that, above the giant resonance region, the (γ,p) cross section calculated in the IPM and in RPA are similar while the (γ,n) results are quite different. Since our model cannot describe collective excitations, we restricted our investigation to the (γ,p) reaction above the giant resonance. Following the treatment commonly adopted to describe the (e,e'p) reactions, we have used an energy dependent optical potential to treat the FSI.

With this model we have investigated the role of the various terms of the electromagnetic current. We studied the difference between electron and photon scattering processes by considering the transverse response at fixed energy for various values of the momentum transfer. We found that at the photon point ($q = \omega$) the response is strongly dominated by the convection current, while with increasing q the magnetization current becomes quickly more important. However, even at the photon point it is not possible to neglect the magnetization current for energies above 100 MeV.

The MEC have been analyzed following the model of Ref. [22], where the pion-exchange diagrams of Fig. 1, labelled as seagull, pionic and Δ, have been included. The use of the seagull diagram only, as it is done in Ref. [75, 76], overestimates the MEC effects. The inclusion of the pionic diagram reduces this effect, and the Δ current is important only for photon energies above 100 MeV. At these energies, a large difference between cross sections calculated with OB currents only and those obtained with the inclusion of the MEC is found for large emission angles.

Our SRC calculations have been done with three different correlation functions taken from the FHNC calculations of Refs. [8, 9]. As already shown for the electron scattering case [16, 17], the effects of two- and three-point diagrams have opposite sign. We observed that the photoemission cross sections show larger sensitivity to the correlations than the electron scattering cross sections. This is due to the different momentum dependences of the transition matrix elements of the IPM and of those containing the correlation function. The IPM transition matrix elements have a sharp rise, while the other ones are almost flat. At the photon point the difference between the two transition matrix elements is relatively smaller than at higher values of the momentum transfer. This is the source of this relatively high sensitivity.

We found that at excitation energies above 150 MeV, the cross sections obtained in the IPM plus OB currents framework, have a sharp decrease for large values of the nucleon emission angle. In this region, the correlations produce cross sections order of magnitude larger than the IPM ones. This is exactly the same, well known, behavior of the nucleon momentum distribution. In effect, converting the emission angle value with the initial momentum of the emitted nucleon, it is possible to verify that IPM and correlated cross section start to separate at about 600 MeV/c, where also the momentum distributions of ^{16}O start to separate. Unfortunately, in these cross sections the MEC play an important role, more important than that of the SRC. Therefore the effect of SRC is overwhelmed by that of the MEC.

The comparison with the data improves when a spectroscopic factor is used. We fixed the value of 0.8 for the $1p_{1/2}$ proton emission, by applying our model to the $^{16}O(e,e'p_0)^{15}N$ data taken at NIKHEF [68]. The same spectroscopic factor value has been used to describe the coincidence electron scattering data taken at Mainz [78] and the photon emission data available in the literature. The inclusion of this reduction factor greatly improves the agreement with all the data sets, in spite of the fact that the factor was extracted for relatively low values of the missing momentum.

We would like to conclude by mentioning some possible way of improving our model. A first one is related to the treatment of the MEC. The energy values of interest is above the pion emission threshold. One may claim that this channel has just open and therefore it is negligible, but one would like to have an estimate of its relevance. A second possible improvement is related to the optical potential at present taken from literature. In a more consistent description the potential should be related to the same nuclear structure model producing the SRC.

References

[1] A. N. Antonov, P. E. Hodgson and I. Zh. Petkov, *Nucleon Momentum and Density Distributions*, Clarendon Press, Oxford, 1988.

[2] J. G. Zabolitzky and W. Ey, *Phys. Lett. B* **76** (1978), 527; M. Dal Rì, S. Stringari and O. Bohigas, *Nucl. Phys. A* **376** (1982), 81; F. Dellagiacoma, G. Orlandini and M. Traini, *Nucl. Phys. A* **393** (1983), 95; O. Benhar, C. Ciofi degli Atti, S. Liuti and G. Salmè, *Phys. Lett. B* **177** (1986), 135; S. Stringari, M. Traini and O. Bohigas, *Nucl. Phys. A* **516** (1990), 33. C. Ciofi degli Atti, E. Pace and G. Salmè, *Phys. Rev. C* **43** (1991), 1155.

[3] F. Arias de Saavedra, G. Co' and M.M. Renis, *Phys. Rev. C* **55** (1997), 673.

[4] A. Fabrocini and G. Co', *Phys. Rev. C* **63** (2001), 044319.

[5] B.S. Pudliner, V.R. Pandharipande, J. Carlson, S. C. Pieper and R. B. Wiringa, *Phys. Rev. C* **56** (1997), 1720.

[6] S. Pieper, R. B. Wiringa and V.R. Pandharipande, *Phys. Rev. C* **46** (1992), 1741.

[7] J. H. Heisenberg and B. Mihaila, *Phys. Rev. C* **59** (1999), 1440.

[8] F. Arias de Saavedra, G. Co', A. Fabrocini and S. Fantoni, *Nucl. Phys. A* **605** (1996), 359.

[9] A. Fabrocini, F. Arias de Saavedra and G. Co', *Phys. Rev. C* **61** (2000), 044302.

[10] G. E. Brown and G. Jacob, *Nucl. Phys. A* **42** (1963), 177; F.C. Khanna, *Phys. Rev. Lett.* **20** (1968), 871; W.J. Gerace and D.A. Sparrow, *Phys. Lett. B* **30** (1969), 71;

C. Ciofi degli Atti and N.M. Kabachnik, *Phys. Rev. C* **1** (1971), 809. M. Gaudin, J. Gillespie and G. Ripka, *Nucl. Phys. A* **176** (1971), 237.

[11] G. Co', *Nuov. Cim. A* **108** (1995), 623.

[12] M. Anguiano and G. Co', to be published in *J. Phys. G*, (lanl:arXiv:nucl-th/0108065).

[13] G. Co' and A. M. Lallena, *Phys. Rev. C* **57** (1998), 145.

[14] J.E. Amaro, A.M. Lallena, G. Co' and A. Fabrocini, *Phys. Rev. C* **57** (1998), 3473.

[15] S.R. Mokhtar, G. Co' and A.M. Lallena, *Phys. Rev. C* **62** (2000), 067304.

[16] G. Co' and A. M. Lallena, *Ann. Phys.* (N.Y.) **287** (2001), 101.

[17] S. R. Mokhtar, M. Anguiano, G. Co' and A. M. Lallena, *to be published on Ann. Phys.* (N.Y.), (lanl:arXiv:nucl-th/0105059).

[18] S. Fantoni and V. R. Pandharipande, *Nucl. Phys. A* **473** (1987), 234.

[19] A. Fabrocini and S. Fantoni, *Nucl. Phys. A* **503** (1989), 375; O. Benhar, A. Fabrocini and S. Fantoni, *Nucl. Phys. A* **550** (1992), 201; A. Fabrocini, *Phys. Rev. C* **55** (1997), 330.

[20] O. Benhar, A. Fabrocini and S. Fantoni, *Nucl. Phys. A* **505** (1989), 267;

[21] J. E. Amaro, G. Co' and A. M. Lallena, *Mean field description of electron induced quasi-elastic excitation in nuclei*, to be published in the book *Quasielastic electron scattering in nuclei*, R. Cenni Ed., Nova Science, (lanl:arXiv:nucl-th 9902072).

[22] J. E. Amaro, G. Co', and A. M. Lallena, *Ann. Phys.* (N.Y.) **221** (1993), 306.

[23] J. E. Amaro, G. Co', and A. M. Lallena, *Nucl. Phys. A* **578** (1994), 365.

[24] M. M. Giannini and G. Ricco, *Riv. Nuovo Cim.* **8** (1985), 1.

[25] J. M. Blatt and V. F. Weisskopf, *Theoretical Nuclear Physics*, John Wiley & Sons, New York, 1952; J. Eisenberg and W. Greiner *Nuclear Theory, vol.2, Excitation Mechanisms of the Nucleus*, North Holland, Amsterdam, 1970.

[26] S. Boffi, C. Giusti, F.D. Pacati and M. Radici, *Electromagnetic Response of Atomic Nuclei*, Clarendon Press, Oxford, 1996.

[27] J.D. Bjorken and S.D. Drell, *Relativistic Quantum Mechanics*, McGraw Hill, New York, 1964.

[28] G. Co' and S. Krewald, *Nucl. Phys. A* **433** (1985), 392.

[29] G. Co', A.M. Lallena and T.W. Donnelly, *Nucl. Phys. A* **469** (1987), 684.

[30] A.R. Edmonds, *Angular momentum in quantum mechanics*, Princeton University Press, Princeton, 1957.

[31] T. De Forest and J. D. Walecka, *Adv. in Phys.* **15** (1966), 1.

[32] G. Hoehler, E. Pietarinen, I. Sabba-Stefabescu, F. Borkowski, G.G. Simon, V.H. Walther and R.D. Wendling, *Nucl. Phys. B* **114** (1976), 505.

[33] M. Chemtob and M. Rho, *Nucl. Phys. A* **163** (1971), 1; J.A. Lock and L.L. Foldy, *Ann. Phys.* (N.Y.) **93** (1975), 276.

[34] J. Hockert, D.O. Riska, M. Gari and A. Huffman, *Nucl.Phys. A* **217** (1973), 14; D.O. Riska, *Mesons in nuclei*, Vol.II, M. Rho and D. Wilkinson, Eds., North-Holland, Amsterdam, 1979.

[35] R.D. Peccei, *Phys. Rev.* **181** (1969), 1902; W.M. Alberico, T.W. Donnelly and A. Molinari, *Nucl. Phys. A* **512** (1990), 541.

[36] J.W. Van Orden and T.W. Donnelly, *Ann. Phys.* (N.Y.) **131** (1981), 451.

[37] D.O. Riska, *Prog. Part. Nucl. Phys.*, **11** (1984), 199; R. Schiavilla, V.R. Pandharipande and D.O. Riska, *Phys. Rev. C* **40** (1989), 2224.

[38] A. Fabrocini, F. Arias de Saavedra, G. Co' and P. Folgarait, *Phys. Rev. C* **57** (1998), 1668.

[39] R. Jastrow, *Phys. Rev.* **98** (1955), 1479.

[40] J. Mayer and M. Mayer, *Statistical mechanics*, Wiley, New York, 1940.

[41] I.R. Afnan and Y.C. Tang, *Phys. Rev* **175** (1968), 1337.

[42] S. R. Mokhtar, *Ph. D. Thesis*, Assiut University, Assiut, Egypt, 2001 (unpublished).

[43] J. E. Amaro, *Ph. D. Thesis*, Granada University, Granada, Spain, 1993 (unpublished).

[44] G. Co', K. F. Quader, R. Smith and J. Wambach, *Nucl. Phys. A* **485** (1988), 61.

[45] S. Drożdż, G. Co', J. Wambach and J. Speth, *Phys. Lett. B* **185** (1987), 287.

[46] S. Boffi, C. Giusti and F.D. Pacati, *Phys. Rep.* **226** (1993), 1.

[47] M. Cavinato, M. Marangoni, P.L. Ottaviani and A.M. Saruis, *Nucl. Phys. A* **373** (1982), 445.

[48] M. Cavinato, M. Marangoni and A.M. Saruis, *Nucl. Phys. A* **422** (1984), 237.

[49] A.M. Saruis, *Phys. Rep.* **235** (1993), 57.

[50] J. Ryckebusch, M. Waroquier, K. Heyde and D. Ryckbosch, *Phys. Lett. B* **194** (1987), 453.

[51] J. Ryckebusch, *Ph. D. Thesis*, Gent University, Gent, Belgium, 1987 (unpublished).

[52] J. Ryckebusch, M. Waroquier, K. Heyde, J. Moreau and D. Ryckbosch, *Nucl. Phys. A* **476** (1988), 237.

[53] R. De Haro, S. Krewald and J. Speth, *Nucl. Phys. A* **388** (1982), 265.

[54] D. Pines, K.F. Quader and J. Wambach, *Nucl. Phys. A* **477** (1988), 365.

[55] J. Ahrens *et al.*, *Nucl. Phys. A* **251** (1975), 479.

[56] J. Speth and J. Wambach, in *Electric and Magnetic Giant Resonance in Nuclei*, J. Speth Ed., World Scientific, Singapore, 1991.

[57] S. Drożdż, S. Nishizaki, J. Speth and J. Wambach, *Phys. Rep.* **197** (1990), 1.

[58] G. F. Bertsch, P. F. Bortignon and R. A. Broglia, *Rev. Mod. Phys.* **55** (1983), 287; G. Colò, P. F. Bortignon, N. Van Giai, A. Bracco and R. A. Broglia, *Phys. Lett. B* **276** (1992), 279; G. Colò, N. Van Giai, P. F. Bortignon and R. A. Broglia, *Phys. Rev. C* **50** (1995), 1496;

[59] S. Kamerdhziev and J. Speth, *Nucl. Phys. A* **599** (1996), 373c; S. Kamerdhziev, J. Speth and G. Tertychny, *Nucl. Phys. A* **624** (1997), 328.

[60] D.J.S. Findlay and R.O. Owens, *Nucl. Phys. A* **279** (1977), 385.

[61] F. De Smet, H. Ferdinande, R. Van de Vyver, L. Van Hoorebeke, D. Ryckbosch, C. Van den Abeele, J. Dias and J. Ryckebusch, *Phys. Rev. C* **47**(1993), 652.

[62] G.J. Miller *et al.*, *Nucl. Phys. A* **586** (1995), 125.

[63] H. Göringer, B. Schoch and G. Lührs, *Nucl. Phys. A* **384** (1982), 414.

[64] M. Buballa, S. Drożdż, S. Krewald and J. Speth, *Ann. Phys.* (N.Y.) **208** (1991) 346. S. Jeschonnek, A. Szczurek, G. Co' and S. Krewald, *Nucl. Phys. A* **570** (1994), 599.

[65] S. Boffi, F. Cannata, F. Capuzzi, C. Giusti and F.D. Pacati, *Nucl. Phys. A* **379** (1982), 509

[66] S. Boffi, R. Cenni, C. Giusti and F.D. Pacati, *Nucl. Phys. A* **420** (1984), 36.

[67] P. Schwandt, H.O. Meyer, W.W. Jacobs, A.D. Bacher, S.E. Vigdor, M.D. Kaitchuck and T.R. Donoghue, *Phys. Rev. C* **26** (1982), 55.

[68] M. Leuschner, J. Calarco, F.W. Hersman, E. Jans, G.J. Kramer,L. Lapikás, G. van der Steenhoven, P.K. de Witt Huberts, H.P. Blok, N. Kalantar-Nayestanaki, and J. Friedrich, *Phys. Rev. C* **49** (1994), 955.

[69] J.P. Jeukenne, A. Lejeune and C. Mahaux, *Phys. Rep.* **25** (1976), 83.

[70] S. Fantoni, B. L. Friman and V. R. Pandharipande, *Nucl. Phys. A* **399** (1983), 51.

[71] G.S. Adams, E.R. Kinney, J.L. Matthews, W.W. Sapp, T. Soos, R.O. Owens, R.S. Turley and G. Pignault *Phys. Rev. C* **38**(1988), 2771.

[72] M. Gari and H. Hebach, *Phys. Rep.* **72** (1981), 1.

[73] J. Ryckebusch, K. Heyde, L. Machenil, D. Ryckbosch, M. Vanderhaeghen and M. Waroquier, *Phys. Rev C* **46** (1992), R829.

[74] J. Ryckebusch, L. Machenil, M. Vanderhaeghen, V. Van der Sluys and M. Waroquier, *Phys. Rev C* **49** (1994), 2704.

[75] G. Benenti, C. Giusti and F.D. Pacati *Nucl. Phys. A* **574** (1994), 716.

[76] M.K. Gaidarov, K.A. Pavlova, A.N. Antonov, M.V. Stoitsov, S.S. Dimitrova, M.V Ivanov and C. Giusti, *Phys. Rev. C* **61** (2000), 014306.

[77] M.J. Leitch, J.L. Matthews, W.W. Sapp, C.P. Sargent, S.A. Wood, DJ.S. Findlay, R.O. Owens and B.L. Roberts, *Phys. Rev. C* **31** (1985), 1633.

[78] K.I. Blomqvist *et al.*, *Phys. Lett. B* **344** (1995), 85.